Journal of Sol-Gel Science and Technology (2026) 118:54
https://doi.org/10.1007/s10971-026-07183-3

ORIGINAL PAPER

The role of individual Er and Tb incorporation in CO_2 gas-sensing properties of hydrothermally grown ZnO nanorods

Fatih Bulut[1,2] · Özgür Öztürk[3] · Şükrü Çelik[4] · Gürcan Yıldırım[5] · Selim Acar[6]

Received: 1 March 2026 / Accepted: 24 April 2026 / Published online: 22 May 2026

Abstract

This study systematically investigated the role of independently doped Erbium (Er) and Terbium (Tb) incorporation on the structural, morphological, optical, and carbon dioxide (CO_2) gas-sensing properties of ZnO nanorods synthesized by the hydrothermal method with dopant concentrations of 0, 1, 3, 5, and 7 wt%. X-ray diffraction (XRD) analysis confirmed the successful substitutional incorporation of Er and Tb ions into the ZnO lattice, preserving the hexagonal wurtzite structure without the formation of secondary phases, except at the highest Tb concentration. These findings are in good agreement with scanning electron microscopy (SEM) results, which revealed vertically aligned ZnO nanorods with uniform spatial distribution and apparent diameters below 100 nm. Further, dopant incorporation significantly influenced nanorod morphology and interfacial characteristics, including variations in diameter uniformity, surface charge homogeneity, and ZnO shell composition and thickness due to differences in ionic radii, valence states, and outer-shell electron configurations of the Er^{3+} and Tb^{3+} dopant ions. This modified local strain fields and defect chemistry within the ZnO matrix. Optical characterization also showed a systematic reduction in optical bandgap energy with increasing dopant content. This is consistent with bandgap narrowing induced by enhanced carrier concentration and defect-related band tailing, accompanied by noticeable changes in optical transmittance. CO_2 gas-sensing experiments displayed that rare-earth doping markedly enhanced sensor performance compared to that of undoped ZnO nanorods. In particular, 5 wt% Er-doped semiconductor exhibited the highest sensitivity, along with rapid response and recovery times, indicating an optimal balance between surface reactivity, charge transport, and defect-mediated adsorption-desorption dynamics. To sum up, the experimental results and theoretical approach obtained highlighted Er- and Tb-doped ZnO nanorods as promising low-cost, chemically stable, and high-performance sensing materials for CO_2 detection in environmental and industrial monitoring applications.

✉ Fatih Bulut
fatihbulut@sinop.edu.tr

[1] Department of Physics, Faculty of Arts and Science, Sinop University, Sinop, Türkiye

[2] Scientific and Technological Research Applications and Research Center, Sinop University, Sinop, Türkiye

[3] Department of Electrical and Electronics Engineering, Kastamonu University, Kastamonu, Türkiye

[4] Department of Energy Systems Engineering, Sinop University, Sinop, Türkiye

[5] Department of Mechanical Engineering, Bolu Abant Izzet Baysal University, Bolu, Türkiye

[6] Department of Physics, Science Faculty, Gazi University, Ankara, Türkiye

Graphical Abstract

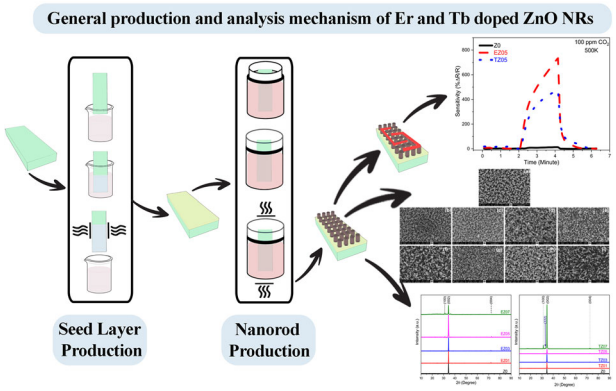

Keywords Gas sensing · ZnO · Tb doped · Er doped · Nanorods · Hydrothermal method

Highlights

- Vertically aligned ZnO nanorods were synthesized using sol-gel seeding and hydrothermal methods.
- Structural changes caused by Er and Tb doping were systematically investigated.
- Wurtzite crystal structure was confirmed by XRD, and surface morphology and hexagonal NR structure were confirmed by SEM.
- It was shown that CO_2 gas detection sensitivity was increased with Er and Tb doping.
- Specific optimum doping levels (e.g., EZ05, TZ05) were determined for performance optimization.

1 Introduction

Glacial data show a long-term relationship between atmospheric CO_2 concentrations and global temperature; CO_2 changes have generally followed the changing of temperature. The delay in tracking is attributed to slow vertical mixing in the oceans and changes in CO_2 solubility [1, 2]. Continuous high-sens measurements initiated at Mauna Loa in 1958 confirm a steady climb in CO_2 concentrations, subject to seasonal cycles. By breaking the atmospheric heat balance, this excess CO_2 induces a rise in near-surface temperatures; a process that is further concentrated by water vapor feedback. Based on these dynamics, carbon dioxide is regarded as the central agent responsible for past and present ecological transformations [3, 4].

The greenhouse gas effect, resulting from human and industrial activities, threatens all life on Earth by causing global climate change. The use of fossil fuels in energy production and many other areas leads to the emission of high amounts of carbon dioxide (CO_2) gas, which is considered one of the primary causes of the greenhouse effect. This gas, which absorbs short-wavelength radiation reflected from the Earth, causes an increase in the Earth's temperature [5]. In addition to its global impact, on a smaller scale, the accumulation of this gas in enclosed spaces can lead to respiratory difficulties, asthma, allergies, and dizziness. Carbon dioxide accumulation, frequently encountered in environments such as mines, is a situation that needs to be monitored for its impact on human health. Also, carbon dioxide gas monitoring and tracking are required in factories producing chemical products, carbonated beverages, and fertilizers, as well as in medical centers using incubators [6–8]. Following the COVID-19 pandemic, CO_2 detectors have become an essential safety requirement for monitoring indoor air quality in many work environments because these are environments where many people need to be or work together [9]. Directly measuring aerosols containing viruses is difficult and time-consuming. Therefore, CO_2 concentrations are used as an indicator of ventilation in indoor spaces; this method was suggested in the 1800s. In recent years, researchers have proposed that monitoring CO_2 levels can act as a surrogate for assessing the risk of airborne infectious diseases, given that viruses and CO_2 are expelled simultaneously. Thus, the implementation of low-cost CO_2 sensors offers a viable method for indirectly tracking indoor infection hazards [9–11].

Per ASHRAE (American Society of Heating, Refrigerating and Air-Conditioning Engineers) guidelines, the recommended CO_2 concentration thresholds are set at 350 ppm for outdoor air and 1000 ppm for indoor spaces [6–8]. Carbon dioxide is one of the most well-known gases, but it is chemically too stable to be accurately detected by

conventional gas sensors. However, the control or measurement of CO_2 concentration is critical in various advanced technologies such as air conditioning, agriculture, biological technology and medical services [12]. Efforts are focused on developing 2D gas sensors using materials such as graphene, phosphorene, boron nitride, and layered metal oxides, as well as on outstanding properties among metal-free 2D semiconductor materials [13].

Gas sensors play a critical role in the detection and monitoring of pollutant gases that pose a danger to human and environmental health. Air pollution has become a significant global environmental problem today due to the rapid increase in industrialization and urbanization [14, 15]. In recent years, production methods for gas sensors with high sensitivity, high accuracy, low operating temperature, and low cost have become widespread. While older generation gas sensors had limited applications due to their high voltage requirements (20–100 V) and high operating temperatures (300–700 °C), today compact sensors with low energy consumption are coming to the forefront in this field [16–20].

The use of wide-bandgap semiconductors in advanced technological applications has increased steadily in recent years [21]. Among these materials, ZnO-based semiconductors are particularly attractive for gas-sensing applications owing to their low cost, compatibility with diverse fabrication techniques, environmental friendliness, and excellent thermal and chemical stability [22–24]. Although the inherently high surface area of ZnO nanostructures favors enhanced gas-sensing performance, further modification is required to achieve higher sensitivity and reduced operating temperatures [25]. Zinc oxide semiconductor thin films, which are reported as 3.37 eV direct band gap, display tunable physical and electronic properties, making the materials attractive for various applications [26, 27]. The adjustable properties of ZnO films provide advantages such as ease of use in different applications, cost-effectiveness, and simple production processes [28]. Particularly, ZnO nanorods have become a frequently preferred material for gas detection applications in recent years due to their large surface area and superior optical, electrical, and chemical properties [29–33]. Recent advancements highlight that one-dimensional (1D) metal-oxide nanostructures are rapidly evolving from fundamental research platforms into practical, scalable sensor devices that offer long-term stability and robust selectivity [34, 35]. For instance, 1D ZnO nanotubes synthesized via chemical bath deposition have demonstrated outstanding chemiresistive performance, detecting NO_2 gas at concentrations as low as 1 ppm at 200 °C with rapid response times and huge stability over 40 days [36]. In another notable study, highly asymmetric 1D ZnO nanostructures, such as nanowires and nanobelts, achieved an ultra-low detection limit of 50 ppb for formaldehyde vapor, a performance directly attributed to their polar surface morphologies and defect-induced adatom migration [37]. This structure-defect relationship is further emphasized in vapor-phase grown 1D sulfur-doped ZnO nanostructures, where increased surface oxygen vacancies-evidenced by strong visible photoluminescence (PL)-significantly accelerating adsorption-desorption dynamics, boosting acetone gas sensitivity up to 85% and drastically reducing response times [38]. Similarly, recent investigations into 1D ZnO nanowires and nanorods synthesized via vapor-liquid-solid techniques demonstrate that such oxygen vacancy point defects play a critical role in achieving a high sensing response of approximately 80% and rapid detection times specifically for CO_2 gas. Furthermore, the versatile surface defect chemistry of these 1D ZnO nanostructures enables their exceptional sensing capabilities to extend even beyond volatile gases to the trace-level detection of heavy metal ions like Cu^{2+} and Fe^{3+} in aqueous environments [39].

Despite the potential for morphological optimization through various synthesis techniques, effective tuning of electrical conductivity (the most critical parameter in chemiresistive gas sensors) requires targeted approaches such as the incorporation, substitution, or diffusion of suitable anionic and cationic species into the crystal lattice. Among the techniques, the doping scheme enables the modification of electronic, chemical, and morphological properties [40]. Even the use of dopants has already been common in improving the electrical conductivity and gas sensing performance of semiconductors. Today, the dopant elements are generally selected from rare earth elements due to the special energy structure of their 4 f electron shells and their effects on oxygen vacancies. As in the literature, doping ZnO with rare-earth elements such as erbium (Er) and terbium (Tb) enables the deliberate introduction of controlled impurity levels that promote electron-hole pair generation within the host lattice [33, 40–43]. Owing to their trivalent oxidation state (Er^{3+}, $4f^{11}$), these dopant ions can partially substitute Zn^{2+} sites and be incorporated into the ZnO crystal structure, where Er^{3+} ions also serve as effective structural and optical probes due to their characteristic intra-4f electronic transitions [44, 45]. However, direct excitation of Er^{3+} ions is a challenging process due to forbidden transitions, phonon-assisted collisions, and emission extinctions [46]. Nevertheless, Erbium-doped semiconductors, based on Si, GaAs, and GaN, have been extensively used in optical applications ranging from the visible to the infrared (IR) spectrum [47, 48]. Erbium, with its closed 5 s and 5p shells providing protection and an incomplete 4 f electronic shell, offers excellent optical properties for the materials to which it is doped [49, 50]. ZnO with a wider band gap value of 3.37 eV and higher electrical conductivity is frequently reported in the literature as a suitable host material for Er doping [45].

As highlighted by Galdámez-Martinez et al., visible deep-level emissions (DLE) in 1D ZnO nanostructures originate from surface-localized point defects that govern molecular adsorption and gas-sensing capabilities [38, 51]. Accordingly, rare-earth doping can deliberately modulate, rather than merely suppress, this defect chemistry. While modifying the overall ZnO lattice [52–55]. Tb incorporation fine-tunes these critical surface defects. The resulting intra-4f transitions of Tb^{3+} ions [56] induce a blue shift and enhance violet-blue emission, reflecting a functional reconfiguration of defect states. By tailoring these surface defect profiles, rare-earth doping optimizes surface reactivity, thereby significantly enhancing the nanorods' chemiresistive gas-sensing performance [57, 58].

Recent research has increasingly highlighted the potential of Er- and Tb-doped ZnO nanostructures for CO_2 gas sensing, although ZnO-based sensors synthesized via different techniques have been investigated to a limited extent [39, 59, 60]. In this work, 1D ZnO nanorods, which inherently possess a high surface-to-volume ratio beneficial for gas sensing, were synthesized using a hydrothermal approach and systematically modified with varying atomic concentrations of Er^{3+} and Tb^{3+} ions. Comprehensive morphological, structural, optical, and CO_2 sensing characterizations were subsequently performed to examine the effects of rare-earth doping on the sensing/recovery performance, interfacial electrostatic charges, and underlying material properties, including structural, morphological, and optical features.

2 Experimental procedure

2.1 Production method

ZnO nanorods doped with 0, 1, 3, 5, and 7 wt% of Er^{3+} and Tb^{3+} ions were produced by the hydrothermal method. First, a seed layer was coated on glass substrates, which were previously cleaned with acetone (CH_3COCH_3), ethanol (CH_3CH_2OH), and distilled water for 10 min. each in an ultrasonic bath, using the dip-coating method. Ideally, the seed layer dictates the formation and alignment of the nanorod structures. The dip-coating solution was prepared by dissolving Zinc Acetate dihydrate (CAS: 5970-45-6, MERCK, $Zn(CH_3COO)_2$-$2H_2O$) and methanol (CAS: 67-56-1, MERCK, CH_3OH) in monoethanolamine (CAS: 141-43-5, MERCK, $NH_2CH_2CH_2OH$). The deposition consisted of 5 dips on the cleaned substrates, with heat treatments at 300 °C between each dip. The films were subsequently annealed at 600 °C for a duration of 30 min. to complete the crystalline ZnO seed structure. After preparing the seed layer process, a 10 mM growth solution was ready for hydrothermal synthesis. Zinc Acetate dihydrate was dissolved in deionized water at room temperature to form a clear and homogenous solution. Calculated amounts of Erbium(III) acetate hydrate (CAS: 207234-04-6, MERCK, $(CH_3CO_2)_3Er$-xH_2O) and Terbium(III) acetate hydrate (CAS:100587-92-6, MERCK, $Tb(CH_3CO_2)_3$-xH_2O) were added as doping ions. This solution was followed by the addition of hexamethylenetetramine (CAS: 100-97-0, MERCK, $C_6H_{12}N_4$) equimolar to Zinc Acetate (1:1) to the mixture, which dissolved completely.

During the hydrothermal reaction, the substrates with seed layers were immersed vertically in the solution within Teflon autoclaves. These vessels were placed in a furnace at 90 °C and incubated for 3 h. Post-synthesis, the ZnO nanorod-coated glasses were cooled to room temperature on their own, thoroughly rinsed with deionized water, dried, and heat-treated at 400 °C for 30 min. to improve crystallinity [61–63]. The samples produced were named EZ01, EZ03, EZ05, EZ07, TZ01, TZ03, TZ05, and TZ07 according to the additive element and its ratios, such as 0, 1, 3, 5, and 7wt%; the additive-free control sample was designated as pure or Z0 material.

2.2 Characterization methods

Structural characterization of the synthesized samples was performed at room temperature using a Bruker D8 Advance diffractometer with a CuK_α source with the wavelength of 1.5406 Å over the 2θ ranges of 10–90^0. To examine the surface features and apparent diameters of the nanorods, a scanning electron microscope (FEI Quanta FEG 250) was used. Optical properties and band gap energies were obtained from transmittance spectra recorded in slow mode at a threshold of 0.01 between 350–1100 nm wavelengths using a SHIMADZU 1280 model UV-Vis spectrophotometer. XRD, SEM, and UV characterizations for crystallinity quality, surface appearance, nanorod morphology, interfacial characteristics, crystallization mechanism, texturing, defect-related bond tailing, recovery times, and defect-mediated adsorption-desorption dynamics were performed at the Kastamonu University Central Research Laboratory. In addition, gas detection experiments were carried out in the "gas sensor devices research laboratory" of Gazi University Physics Department. Performed using a Computer-controlled gas sensor measurement system consisting of a Keithley 2400 DC Source Meter, a LakeShore 325 temperature controller, and two MKS Series mass flow controllers that control air and gas flows [62–64].

3 Results and discussion

3.1 XRD analysis

The effects of Er^{3+} and Tb^{3+} ions on the zinc oxide wurtzite crystal structure were systematically investigated by XRD

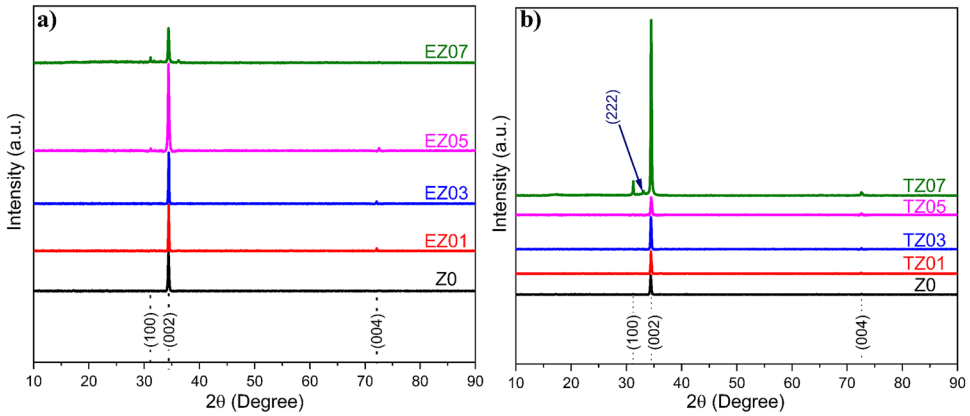

Fig. 1 X-ray diffraction patterns of hydrothermally synthesized ZnO nanorods, showing the wurtzite hexagonal structure, **a** Er doped ZnO, **b** Tb-doped ZnO

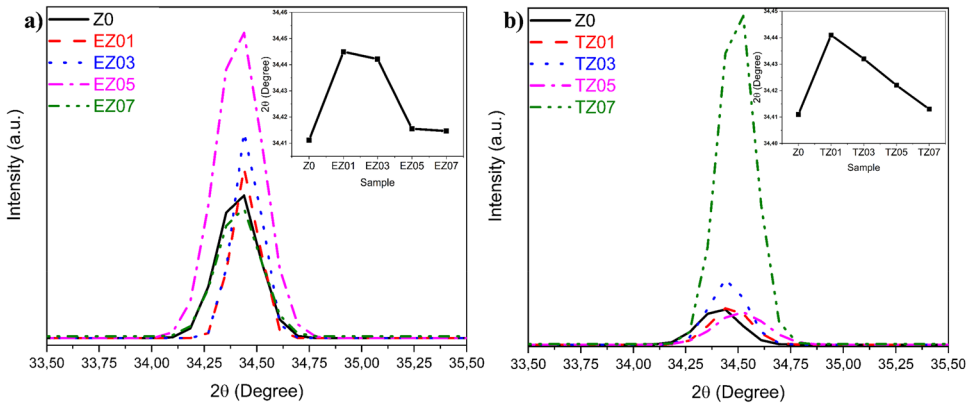

Fig. 2 Shift of the (002) diffraction peak with increasing doping ratio, indicating lattice expansion, **a** Er- doped ZnO, **b** Tb-doped ZnO. Inset raps represent the 2θ degrees obtained by XRD measurement

experiments, focusing on crystallinity, phase purity, c-axis grain orientation, average crystallite size, and lattice parameters. Figure 1 presents the XRD patterns recorded over the 2θ range of 10^0–90^0 at 40 kV and 40 mA, with a step size of 0.05° and a scan rate of 12°/min, where all diffraction peaks are indexed according to their corresponding Miller indices (hkl). The diffractograms reveal that all samples crystallize in the hexagonal wurtzite structure with a dominant (002) preferred orientation, indicating a highly ordered long-range atomic arrangement and strong three-dimensional periodicity [65]. The incorporation of Er^{3+} and Tb^{3+} dopants induces systematic shifts in peak positions and variations in diffraction intensities, displaying estimated lattice parameter variations associated with successful substitution into the ZnO crystal lattice. Importantly, no secondary phases or impurity-related reflections are detected for Er-doped samples, whereas with the sole exception of the TZ07 sample, confirming that both Er and Tb are fully incorporated into the ZnO wurtzite structure without any phase segregation detectable within the resolution limits of our conventional XRD instrumentation. At the excess Tb doping level (TZ07 sample), a weak (222) terbium-related impurity peak is detected, indicating that high Tb concentration adversely affects the crystallization process by increasing the activation energy for crystal growth. This observation displays that 7 wt% Tb doping exceeds the solubility limit and disrupts the ZnO crystal lattice, leading to structural instability and secondary phase formation.

Furthermore, the analysis of angular values reveals that the diffraction peaks shift to lower angles as the Er doping increases (see Fig. 2). The substitution of Zn^{2+} ions with a radius of 74 pm by Er^{3+} ions with an ionic radius of 103 pm causes an increase in interatomic distances in the crystal structure, consequently leading to a decrease in diffraction angle values. Similarly, the substitution of Zn^{2+} ions with Tb^{3+} ions (ionic radius 118 pm) formed the same effect, and diffraction angles shifted to smaller angles [66]. The obtained diffraction patterns are consistent with the ZnO peaks reported in the literature [67–69].

A systematic enhancement in the intensity of the characteristic (002) diffraction peak is observed with increasing dopant concentration, reaching a maximum at x 5 wt% for Er-doped and x = 7 wt% for Tb-doped ZnO samples, indicating improved *c*-axis-oriented crystal growth. Additionally, the emergence of the (100) reflection at $2\theta \approx 31.76^0$ is detected for Er-doped ZnO at x ≥ 5 wt% and for Tb-doped ZnO at x = 7 wt%, indicating dopant-induced modifications in lattice symmetry and crystallite orientation. Besides, the (004) diffraction peak is absent in undoped hydrothermally synthesized ZnO structure; however, it appears at x = 1 wt

Table 1 Crystallite sizes, lattice parameters, band gap and NR diameter of pure and doped ZnO nanorods

Sample	$FWHM_{(002)}$ (^{0})	c (Å)	D (nm)	ε x 10^{-3}	δ x10^{-4} (nm^{-2})	NR Diameter (nm)	Eg (eV)
Z0	0.229	5.208	34.99	3.23	8.17	65.01	3.26
EZ01	0.156	5.203	53.45	2.20	3.50	52.5	3.24
EZ03	0.167	5.203	49.73	2.35	4.04	54.51	3.2
EZ05	0.263	5.208	37.61	3.71	7.07	68.97	3.16
EZ07	0.235	5.208	33.77	3.31	8.77	55.62	3.14
TZ01	0.212	5.204	44.03	2.98	5.16	57.13	3.15
TZ03	0.206	5.205	40.33	2.90	6.15	59.32	3.13
TZ05	0.261	5.207	39.79	3.68	6.32	67.28	3.12
TZ07	0.203	5.208	35.08	2.86	8.13	61.01	3.09

% for both Er- and Tb-doped samples, displaying enhanced crystallinity and long-range ordering along the *c*-axis upon rare-earth incorporation.

In the present study, the prepared samples crystallized in a hexagonal wurtzite structure, and the *c*-axis length for the hexagonal unit cell structure is therefore determined by the following Eq.;

$$\frac{1}{d^2} = \frac{4}{3}\frac{\left(h^2 + hk + k^2\right)}{a^2} + \left(\frac{l}{c}\right) \quad (1)$$

In Eq. 1; d and hkl represent the distances between crystal planes and Miller indices for the respective diffraction planes, respectively, while *a* and *c* are lattice parameters. Simultaneously, the crystal size along the primary growth direction was calculated using the Scherrer formula, which is assessed from XRD patterns. Unlike conventional polycrystalline ZnO thin films exhibiting multiple distinct reflections, highly 1D oriented nanorods (002) show preferential orientation. Since secondary peaks could not be obtained, only the dominant (002) reflection was used to calculate the crystallite size and microstress; this is a well-known approach in the literature for such 1D structures.

$$D = 0.94\lambda/\beta\cos\theta \quad (2)$$

D represents the crystal size, λ the wavelength of the X-ray used for measurement, and θ and β the diffraction angle and FWHM (full width at half maximum) value obtained from the XRD pattern. All obtained data are given in Table 1.

The average particle size calculated using the Scherrer-Warren relation for the pure Z0 sample was found to be 34.99 nm. Significant changes in particle sizes were observed with increasing dopant ratio [70, 71]. Data obtained from XRD analysis are presented in Table 1. The examined particle size values showed a significant increase (53.45 nm for EZ01 and 44.03 nm for TZ01) with 1% doping. Effect of Microstructure compared to the Z0 sample; however, as the doping ratio increased, particle sizes exhibited a decreasing trend and reached 33.77 nm for EZ07 and 35.08 nm for TZ07 samples. It is thought that this observation may be due to the dopant element atoms settling at grain boundaries and dopant-induced structural modulation, thus limiting particle growth [72]. Furthermore, in the present study, quantum confinement effects appear to influence crystallite size evolution, consistent with previous reports [63, 73, 74]. According to the literature, a reduction in crystallite size can induce quantum confinement when the dimensions approach the electron wavelength [73, 75]. In ZnO-based systems, this effect may be further enhanced by the combined influence of reduced crystallite size and increased defect density. However, it should be emphasized that the observed band gap narrowing in this work is predominantly attributed to dopant-induced defect states, lattice strain, and band tailing effects, rather than quantum confinement. Correspondingly, the highest crystallite size is achieved for x = 1% for each substitution system. This behavior is attributed to differences in ionic radius, electronegativity, valence state, outer-shell electron configuration, and dopant-host hybridization mechanisms associated with Er and Tb incorporation into the ZnO lattice. Hence, XRD analysis confirms that while the hexagonal wurtzite structure of ZnO remains structurally intact upon doping, the crystallite sizes are strongly and selectively modified.

The following standard analytical formulas allow us to estimate the relative microstress (ε) and dislocation density (δ) in the ZnO parent crystal structure due to shifts in diffraction peak positions caused by Er and Tb doping;

$$\delta = 1/D^2 \quad (3)$$

$$\varepsilon = \beta/4\,\tan\theta \quad (4)$$

All the calculated ε and δ values are depicted in Table 1 in detail. It is observed that the pure sample possesses 3.23×10^{-3} and 8.17×10^{-4} nm^{-2} for ε and δ parameters, respectively. For Er-doped samples, at low doping rates (1 and 3% Er), the ε and δ values are observed to decrease significantly compared to Z0 ($\delta = 3.50 \times 10^{-4}$ nm^{-2} and

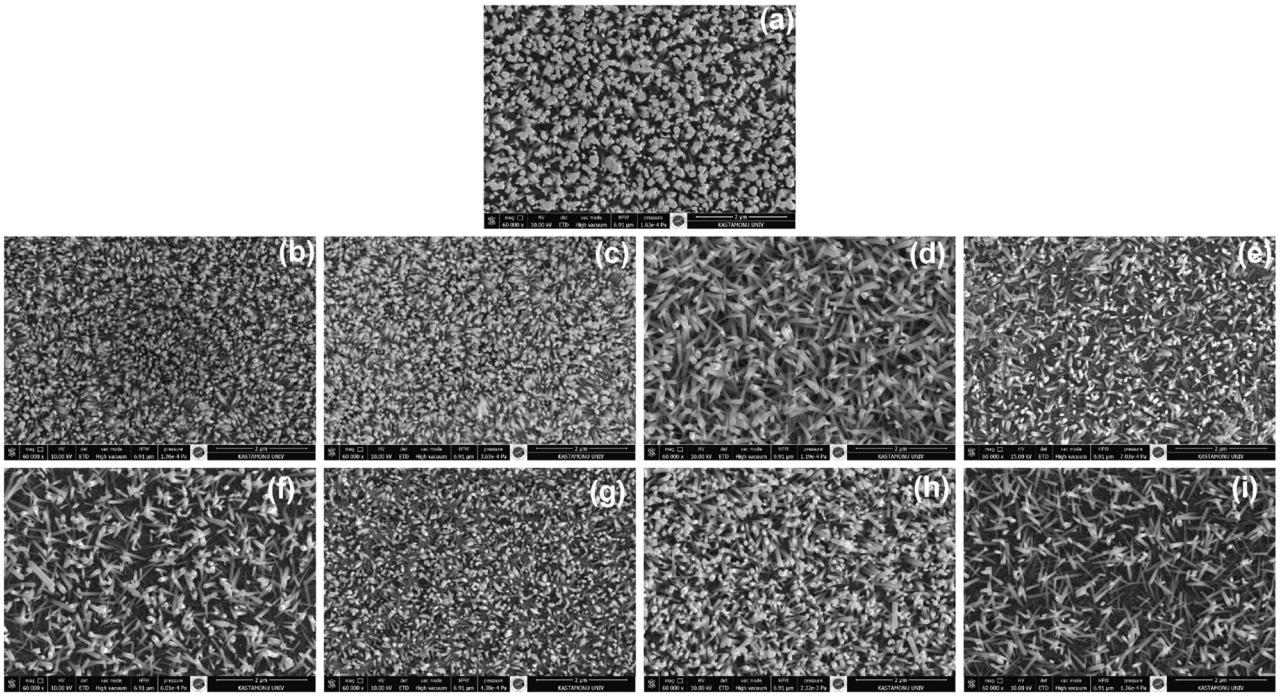

Fig. 3 Multi-panel top-view SEM images of the hydrothermally grown ZnO nanorods: **a** Z0, **b** EZ01, **c** EZ03, **d** EZ05, **e** EZ07, **f** TZ01, **g** TZ03, **h** TZ05, and **i** TZ07. The images illustrate the evolution of nanorod density and surface morphology as a function of Er and Tb doping

$\varepsilon = 2.20 \times 10^{-3}$ for EZ01). This indicates that low Er doping improves crystal quality by reducing internal stress and defect density in the crystal structure. For sample EZ07, both parameters ε and δ are higher than the Z0 sample ($\delta = 8.77 \times 10^{-4}$ nm^{-2} and $\varepsilon = 3.31 \times 10^{-3}$). However, for sample EZ05, parameter ε is higher while parameter δ is lower compared to sample Z0 ($\delta = 7.07 \times 10^{-4}$ nm^{-2} and $\varepsilon = 3.71 \times 10^{-3}$). This shows that excessive Er doping leads to distortion in the crystal structure, increasing stress and dislocation density. The formation of a new peak in XRD already verifies this.

In terbium-doped samples (TZ01, TZ03, TZ05), both ε and δ values are observed to be lower than those in the Z0 reference sample. This suggests that even at a rate of 5%, Tb doping (unlike Er) maintains the overall crystal quality, potentially relaxing internal stress along the c-axis and modulating the local defect chemistry without severe structural degradation. The fact that the δ value in sample TZ07 approaches that of Z0 may indicate the beginning of partial degradation at this rate. High stress and crystal defects are predicted to disrupt the ideal (perpendicular to the c-axis) growth mechanism of nanorods.

3.2 SEM analysis

The morphological properties of the Er and Tb-doped hexagonal wurtzite-type ZnO semiconductors were examined using scanning electron microscopy (SEM) images to obtain detailed information about the general grain size distribution, density, and diameters of the nanorods. Thus, SEM images enable us to determine the alteration of CO_2 sensing performance with Er- and Tb-doped ZnO by modifying operating temperature, sensitivity, charge transport, and surface reaction kinetics. SEM images show that as the Er doping ratio increases, the nanorod density (space between the nanorods) on the sample surface decreases (increases) significantly, as given in Fig. 3, similar to literature [76]. In this respect, the hexagonal wurtzite-type ZnO nanorod structure prepared by 5% Er ions presents a higher response to the CO_2 detection due to the fact that a polycrystalline nanorod structure with a high density of grain boundaries enhances surface adsorption and potential barrier modulation during gas exposure. This improvement is attributed to Er-induced oxygen vacancies and increased electron trapping sites along the crystal system. Excessive Er doping, however, degrades morphology and reduces sensitivity due to surface flattening and reduced active area.

In contrast, such a systematic decreasing density trend was not observed in Tb-doped samples, as provided in Fig. 3. Thus, among the ions, Er doping provides a more stable crystal structure and more efficient gas-surface interaction than Tb doping. At higher Tb concentrations, over-doping leads to crystal degradation and disrupted nanorod morphology, leading to limiting gas-surface interaction despite increased resistance modulation. In fact, in the EZ07 and TZ07 samples, the nanorods on the surface became quite

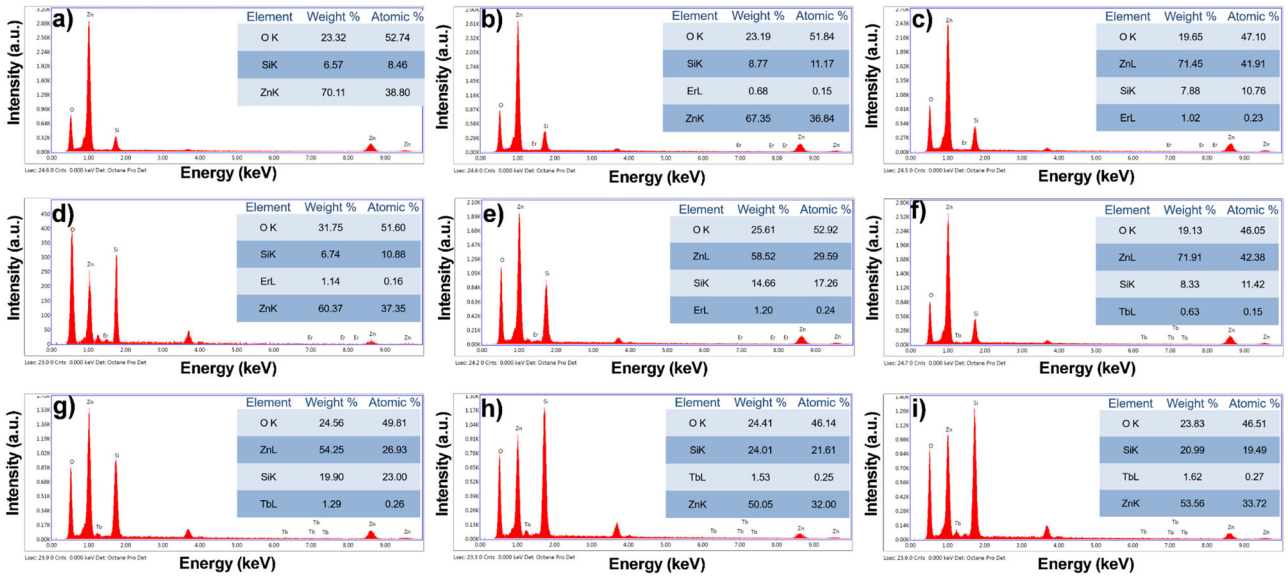

Fig. 4 Point EDS spectra for the corresponding **a** Z0, **b** EZ01, **c** EZ03, **d** EZ05, **e** EZ07, **f** TZ01, **g** TZ03, **h** TZ05, and **i** TZ07 samples. The inset tables provide the quantitative elemental composition (Weight % and Atomic %), confirming successful dopant incorporation and sample purity

infrequent, lost their vertical positions, and exhibited mostly horizontal orientation.

Furthermore, the elemental composition and successful incorporation of the rare-earth dopants were explicitly supported by point EDS analysis, as shown in Fig. 4. The quantitative results in the inset tables confirm the high purity of the synthesized nanorods without any detectable trace impurities.

In more detail, nanorod surface density varies depending on the dopant element and its ratio; apparent diameter values generally remain below 100 nm (See Fig. 5). As the contribution rate increased, an increasing trend was observed in the apparent diameter values calculated by means of histograms, but this trend was disrupted with 7% contribution (Table 1) [77]. The expansion in diameter values, although weak, is supported by the (100) peaks observed in the XRD patterns.

At the same time, except for optimum doping conditions, the tendency of Tb-doped ZnO nanorods to have larger diameters compared to Er-doped ones (except for the optimum level) can be explained here as follows. Tb^{3+} ions induce stronger lattice distortion, defect formation, and surface energy modification during growth, which collectively favor radial over axial growth [56, 78]. Owing to its slightly larger ionic radius (Tb^{3+}, Er^{3+}, and Zn^{2+} ionic radii are nearly 118 pm, 103 pm, and 74 pm, respectively) and stronger tendency to segregate near surface and grain boundary regions, Tb^{3+} more effectively alters the electrostatic environment of ZnO side facets, enhancing host-atom surface diffusion and lateral coalescence. This promotes thickening of the nanorods and results in increased apparent diameter as compared to the presence of Er^{3+} ions. In contrast, Er^{3+} ions are more uniformly incorporated into the ZnO semiconducting lattice system, stabilizing the wurtzite structure and preserving preferential *c*-axis-oriented growth, which limits radial expansion, having already been verified by XRD experiments [79–81]. Consequently, Tb doping shifts the growth kinetics toward lateral enlargement, while Er doping favors slimmer, vertically aligned nanorods.

All in all, both Er and Tb doping induce a non-monotonic evolution of ZnO nanorod morphology governed by the interplay between ionic size mismatch, defect chemistry, surface charge redistribution, and hydrothermal growth kinetics. The morphology optimized at intermediate dopant levels (EZ05 and TZ05) directly correlates with enhanced structural quality and superior CO_2 sensing performance, implying the importance of controlled rare-earth doping in engineering high-performance ZnO-based gas sensors.

3.3 Optical analysis

The optical transmittance spectra of pure and doped ZnO nanorods in the visible region (400–800 nm), presented in Fig. 6, reveal a clear dopant- and concentration-dependent evolution of optical behavior. The undoped ZnO semiconducting sample exhibits the highest transparency, with an average transmittance of ~82% in the visible spectrum (~400–800 nm), indicating its good crystallinity, low defect density, and minimal light-scattering centers. Such high transparency is characteristic of well-aligned ZnO nanorods with smooth surfaces and a relatively low concentration of intrinsic defects.

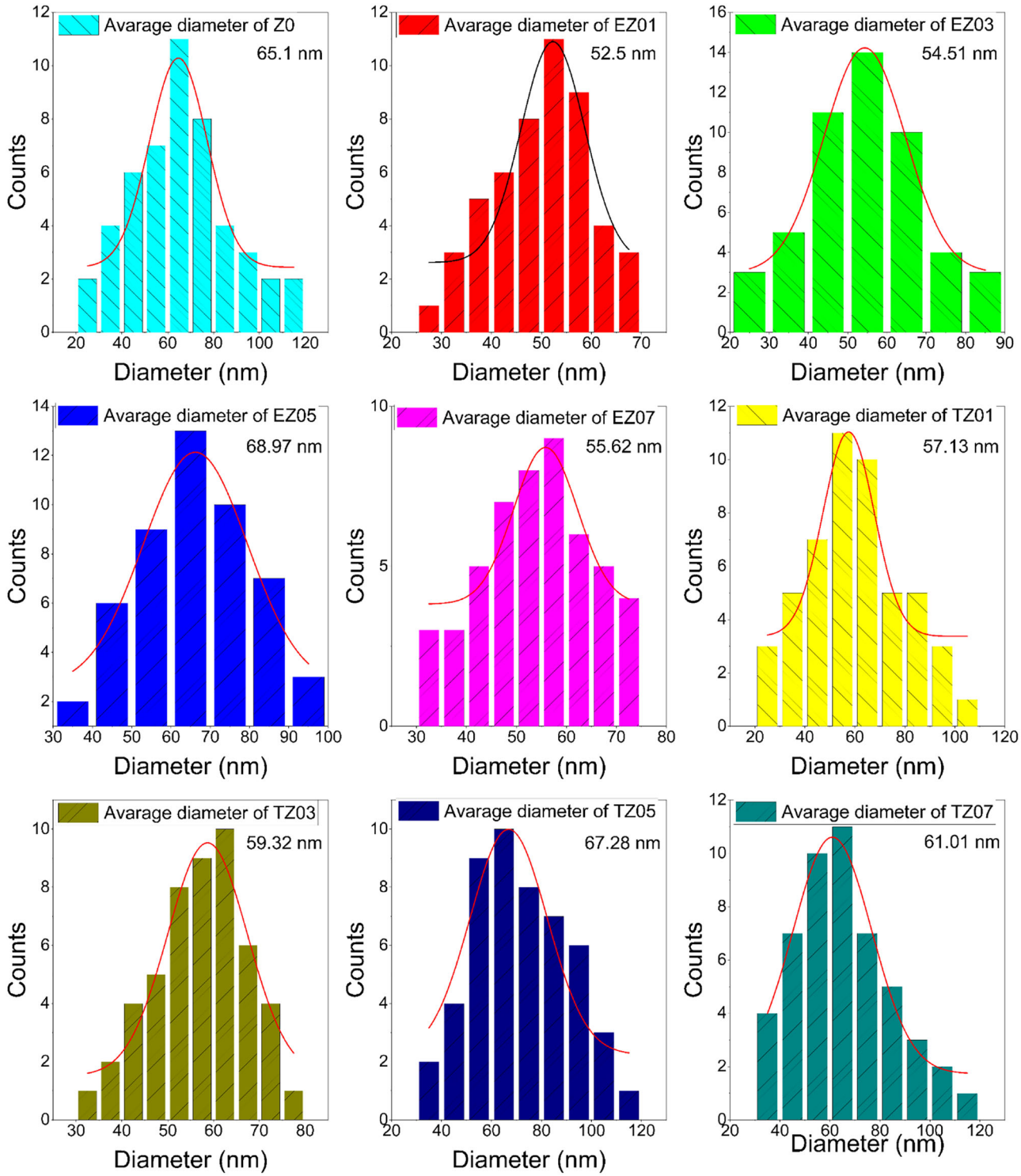

Fig. 5 Apparent diameter distribution histograms of the synthesized nanorods extracted from the SEM analysis for all pure and doped samples

Upon Er incorporation, a strong and systematic reduction in optical transmittance is observed with increasing dopant concentration. Low Er contents (EZ01 and EZ03) cause only a moderate decrease, whereas higher Er loading leads to a substantial loss of transparency, with the EZ07 sample exhibiting transmittance values as low as ~40% [25]. This disruption can be attributed to multiple mechanisms occurring simultaneously: i- increased defect density, particularly oxygen vacancies and zinc interstitials induced by Er^{3+} substitution for Zn^{2+} (perfectly confirmed by XRD

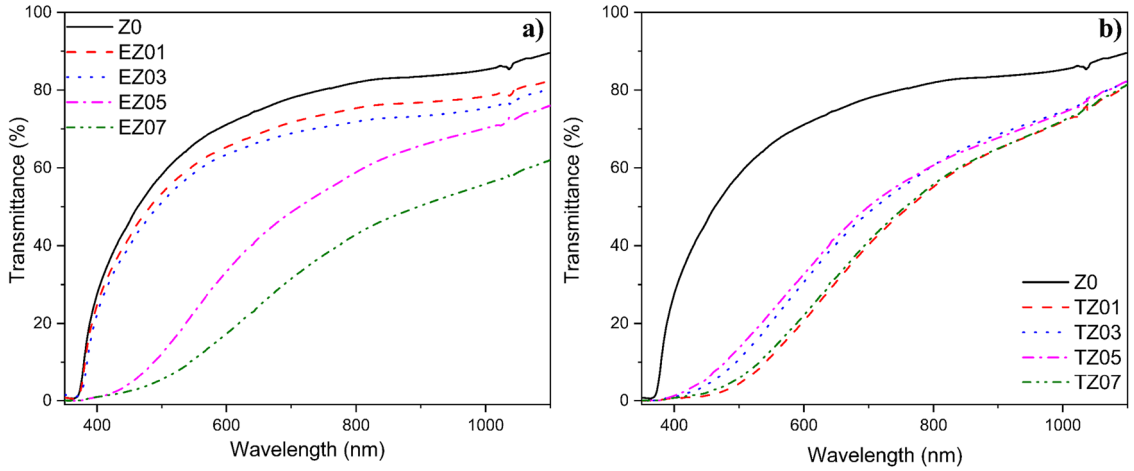

Fig. 6 UV-Vis optical transmittance spectra in the visible range (400–800 nm) demonstrating the effect of **a** Er and **b** Tb doping concentrations on the optical transparency of the ZnO nanorods

measurements) [25, 82, 83], ii- enhanced light scattering resulting from variations of nanorod apparent diameter, density, and surface roughness (corroborated by SEM investigations) [82, 84], and iii- absorption associated with localized 4 f (with special energy structure) electronic states of Er^{3+} ions. Additionally, Er-induced lattice strain and increased grain boundary density act as effective scattering and absorption centers, densification and grain growth [25, 45], further diminishing optical transmission at higher doping levels [25, 45]. In more detail, it is well known that dopants (Mg, Al, and Ga) typically exhibit limited solid solubility in ZnO semiconducting structure, leading to their preferential segregation at grain boundaries and surfaces rather than homogeneous incorporation into the lattice [85–87]. While such segregation can promote nanostructuring and contribute to reduced thermal conductivity, it may also adversely influence carrier transport. Particularly, dopant accumulation at grain boundaries can introduce potential barriers and scattering centers, accordingly affecting charge carrier mobility, electrical conductivity, and the Seebeck coefficient [88–91].

A similar but comparatively smoother trend is observed for Tb-doped ZnO nanorods. Although all Tb-doped samples show lower transmittance (maximum transmittance of ~70%) than the pristine ZnO semiconductor produced in the current work, the variation among different Tb concentrations is less abrupt than in the Er-doped series [92]. This is attributed to a more gradual incorporation mechanism for Tb^{3+} ions and a relatively balanced modification of the ZnO crystal lattice. The reduced transparency in Tb-doped ZnO semiconducting samples is primarily associated with dopant-induced defect states and energy transfer processes between the ZnO host atoms and Tb^{3+} ions, which increase sub-bandgap absorption [65, 93, 94]. Moreover, the larger nanorod apparent diameters observed in Tb-doped samples contribute to enhanced multiple scattering effects, further lowering the transmittance spectra.

To sum up, the reduction in optical transparency with rare-earth doping displays a trade-off between optical and functional properties [95, 96]. While Er and Tb incorporation degrade visible-light transmittance due to increased defect-related absorption and morphological changes, these same features contribute positively to electrical conductivity modulation and gas-sensing performance [78, 83, 97, 98]. Therefore, controlled rare-earth doping enables tuning of ZnO nanorods toward multifunctional applications, where moderate optical losses are acceptable in exchange for enhanced sensing, photoactive characteristics, and electronic characteristics [45, 99].

We also determine the change of optical band gap energy (Eg) values depending on the Er and Tb doping levels in the ZnO semiconducting material by use of Tauc's plot graphics given in Fig. 7, including Planck's constant (h), transition frequency (ν), and absorption coefficient (α). The calculated Eg values are numerically depicted in Table 1. It is seen from the table that the variation of Eg parameters for the ZnO nanorods as a function of Er and Tb doping exhibits a clear and systematic narrowing trend, confirming the effective incorporation of rare-earth ions into the ZnO crystal lattice. This has already been confirmed by SEM and XRD experimental findings. Table 1 shows that the pristine ZnO semiconductor possesses the highest band gap energy of 3.26 eV, in good agreement with reported values for high-quality ZnO nanorods and thin films [99, 100]. Upon Er doping, the Eg parameter is found to decrease monotonically from 3.24 eV (EZ01) to 3.14 eV (EZ07), while Tb doping induces an even more serious reduction, reaching a minimum of 3.09 eV for TZ07 due to increased donor levels in the conduction bands [83, 99]. This

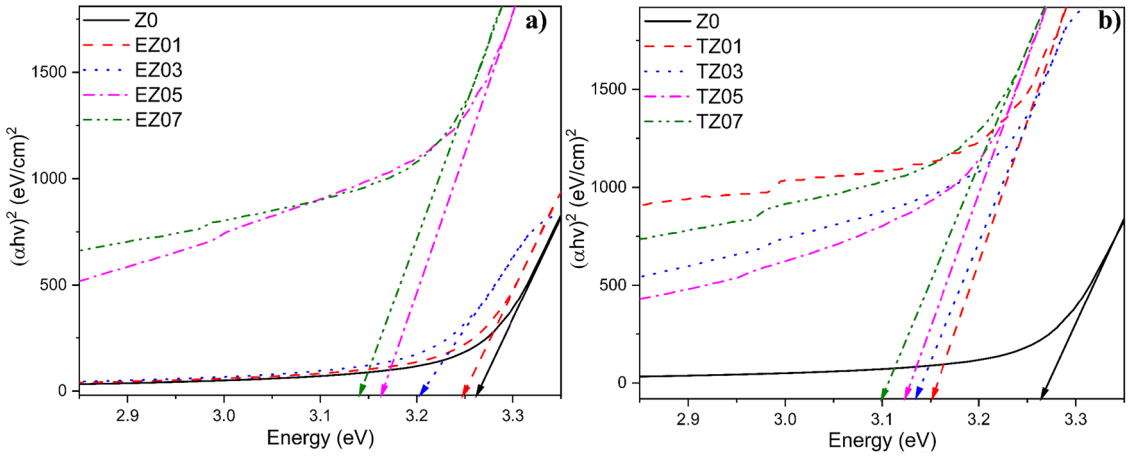

Fig. 7 Tauc plots demonstrating the calculated optical band gap energies (E_g) of the hydrothermally grown ZnO nanorods as a systematic function of **a** Er and **b** Tb doping concentrations

systematic band gap narrowing is primarily attributed to the band shrinkage effect associated with increased carrier concentration arising from dopant-induced defect states, particularly oxygen vacancies and zinc interstitials. This introduces new donor levels near the conduction band [97]. Besides, it should be emphasized here that the charge carrier concentration is not directly quantified using dedicated techniques such as Hall effect measurements, electrochemical impedance spectroscopy (EIS), or detailed photoluminescence (PL) defect-state analysis. Likewise, no advanced electronic structure calculations are performed to explicitly determine carrier density variations. Instead, the evolution of carrier concentration is inferred indirectly from a set of consistent experimental findings. Particularly, the observed systematic band gap narrowing from optical measurements, the pronounced enhancement in CO_2 gas-sensing performance, and the dopant-induced modifications in defect chemistry and microstructure, as evidenced by XRD and SEM analyses, collectively point to an increase in free carrier density. This behavior is attributed to the formation of donor-type defects, such as oxygen vacancies and zinc interstitials, which are well known to act as electron donors in ZnO-based systems. Additionally, the replacement of trivalent Er^{3+} and Tb^{3+} ions for divalent Zn^{2+} particles along the ZnO crystal system both introduces charge imbalance and generates lattice strain and local potential fluctuations, supporting the formation of localized states within the band structure and defect-mediated carrier generation that effectively reduces the optical transition energy as seen in the current work [101].

Morphological factors, such as dopant-dependent changes in nanorod apparent diameter, surface roughness, and oxide layer thickness, further contribute to Eg parameters reduction by modifying quantum confinement conditions and interfacial charge distributions. The slightly lower Eg values observed in Tb-doped samples compared to their Er-doped counterparts can be correlated with stronger lattice perturbation and enhanced sp-f (as compared to sp-d) exchange interactions, which facilitate greater defect-related band tailing [96, 102]. Hence, the monotonic decrease in Eg with increasing Er and Tb content reveals successful dopant incorporation and emphasizes the strong coupling between structural modification, defect chemistry, and electronic band structure in rare-earth-doped ZnO semiconducting nanorods, which is highly beneficial for tuning their optoelectronic and gas-sensing performance [98, 103].

3.4 CO_2 sensing analysis

Determining the optimum operating temperatures of the prepared direct-transition-type ZnO semiconducting materials to be used as gas sensors is critically important for the usability of the sensor technology. The kinetic energy of target gas molecules increases as temperature rises, and this affects the desorption of gas from the sensor surface [62, 104]. Increasing the operating temperature accelerates surface reactions, contributing to obtaining higher sensitivity (S) values. In chemiresistive gas sensors, sensitivity is defined using the following formula:

$$S = \frac{\Delta R}{R_a} = \frac{|R_a - R_g|}{R_a} x100 \quad (5)$$

in the equation, S represents the sensitivity percentage, R_a represents the resistance of the sensor in air environment, and R_g represents the resistance value in gas environment.

Temperature is a crucial parameter determining gas detection performance since it directly affects the kinetic energy of gas molecules and the adsorption-desorption

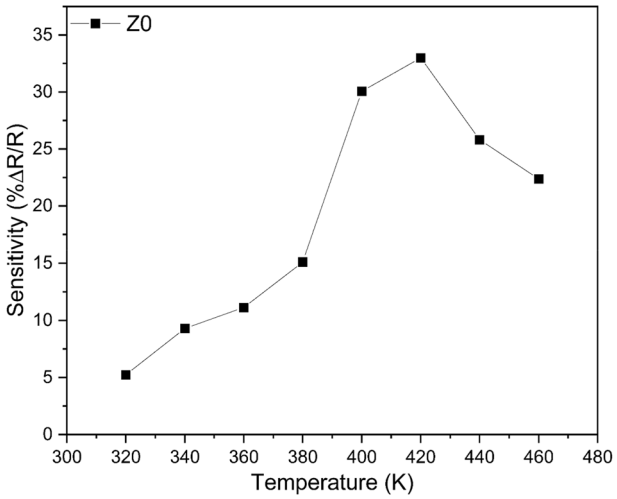

Fig. 8 Temperature-dependent chemiresistive CO_2 gas-sensing response of the pure ZnO (Z0) nanorods evaluated at a fixed gas concentration of 50 ppm to determine the optimal operating temperature

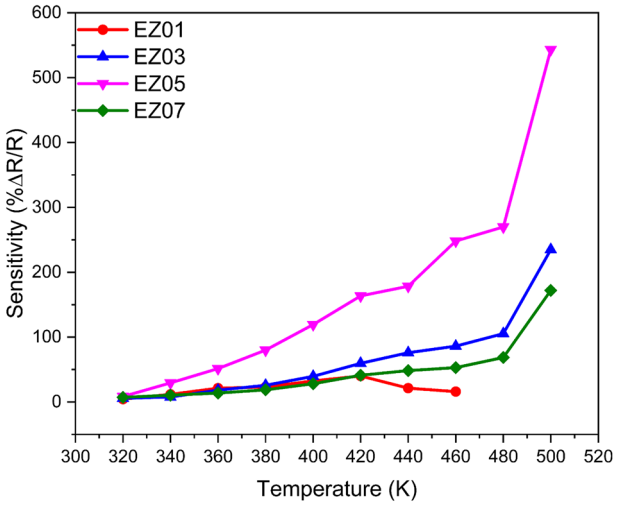

Fig. 9 Temperature-dependent CO_2 gas-sensing response of the Er-doped ZnO nanorods (EZ series) evaluated at 50 ppm

Table 2 Maximum CO_2 sensitivity values of all ZnO nanorods at their optimum operating temperatures

Sample	Z0	EZ01	EZ03	EZ05	EZ07	TZ01	TZ03	TZ05
Operating Temp. (K)	420	420	500	500	500	440	480	500
Response (S) (%)	32	40	234	543	172	113	248	403

dynamics on the sensor surface. An increase in operating temperature does not necessarily lead to enhanced sensitivity; instead, gas sensors often exhibit material-dependent behavior, where sensitivity increases up to a certain temperature and subsequently declines [105]. This response arises from thermally induced changes in surface chemistry, charge transfer processes, and, in some cases, the microstructural stability of the sensing layer. The temperature at which the sensor response reaches its maximum before decreasing is therefore defined as the optimal operating temperature of the sensor, representing a balance between efficient gas adsorption, surface reaction kinetics, and desorption rates [106, 107]. To determine the operating temperatures, CO_2 gas was fixed at a concentration of 50 ppm, and since adequate sensitivity could not be obtained in measurements taken at room temperature, the temperature was increased from 320 K in 20 K intervals and terminated at 500 K. In this regard, Figs. 8–10 present the temperature-dependent CO_2 sensing behavior of pure and rare-earth-doped ZnO nanorods, emphasizing the strong interplay between operating temperature, dopant type, and surface morphology. For the undoped ZnO sample presented in Fig. 8, the sensitivity gradually increases with temperature and reaches a maximum value of ~32% at 420 K (Table 2), beyond which a clear decline is observed. This behavior displays the classical chemiresistive response of ZnO semiconductor, where moderate heating enhances gas molecule activation and surface reaction kinetics, while excess temperatures promote rapid desorption and reduce effective surface coverage. This leads to lower sensitivity.

Additionally, the main temperature-sensitivity characteristics for the Er^{3+}-doped ZnO nanorods are presented in Fig. 9. Compared with the pristine sample, Er doping obviously augments the sensor response and shifts the optimal operating temperature toward higher values. While the EZ01 sample reaches its maximum sensitivity at 420 K, similar to the pure sample, the EZ03, EZ05, and EZ07 semiconductors show their peak responses at around 500 K (Table 2). Among all investigated EZ series, EZ05 with enhanced structural quality displays the highest sensitivity, reaching an outstanding value of 543% (Table 1), indicating the strong promotional effect of optimal Er incorporation on gas-surface interaction. This improvement is attributed to Er-induced oxygen vacancies, increased electron trapping sites, and enhanced modulation of the surface potential barrier. In the SEM images, we have already discussed in detail why the EZ05 sample exhibits the best CO_2 detection performance among the samples examined. In contrast, the sensitivity of EZ07 decreases despite its higher dopant content. Similarly, SEM observations reveal that the presence of excess Er doping in the main matrix leads to sparse, flattened, and less vertically aligned nanorods, which significantly reduces the active surface area available for CO_2 adsorption and weakens the sensing response.

Furthermore, Fig. 10 presents the temperature-dependent CO_2 sensitivity of Tb-doped ZnO nanorods. The TZ01, TZ03, TZ05, and TZ07 samples reach their maximum

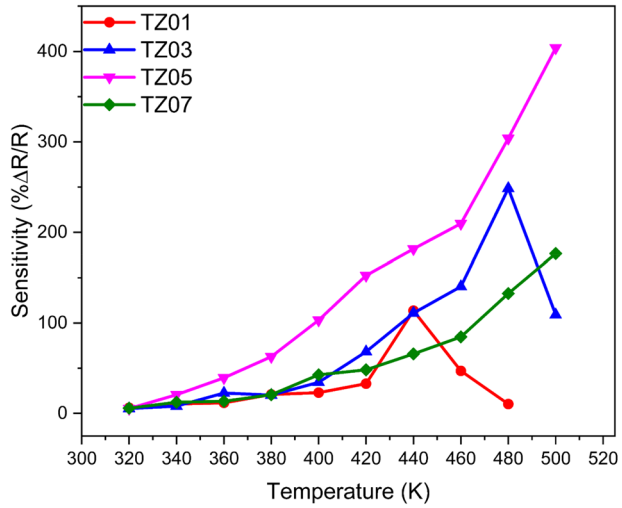

Fig. 10 Temperature-dependent CO_2 gas-sensing response of the Tb-doped ZnO nanorods (TZ series) evaluated at 50 ppm

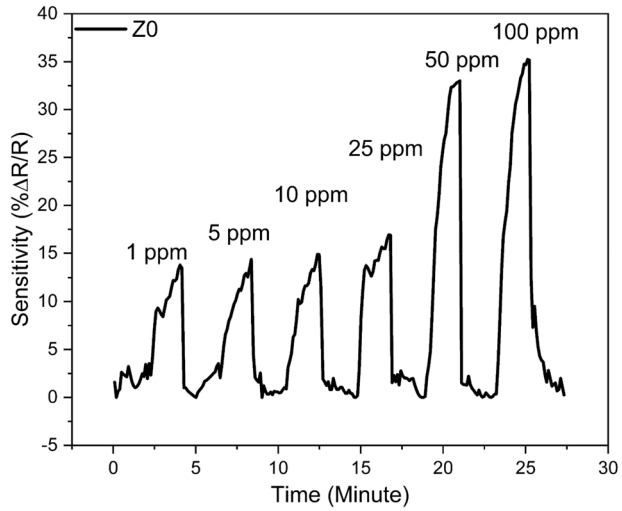

Fig. 11 Dynamic transient gas-sensing response of the pure ZnO (Z0) nanorods exposed to stepwise varying CO_2 concentrations ranging from 1 to 100 ppm at the optimal operating temperature of 420 K

sensitivities at approximately 440, 480, 500, and 500 K (Table 2), respectively, revealing that Tb incorporation also shifts the optimal operating temperature toward higher values. The TZ05 sample exhibits the best performance within the TZ series, achieving a maximum sensitivity of 403% at 500 K, whereas the TZ01 sample shows the lowest response (~ 113%) at 440 K, as given in Table 2. Correspondingly, further increasing the Tb dopant concentration to 7% in the ZnO semiconducting matrix results in a reduced sensitivity. The degradation is associated with dopant-induced structural disorder and degradation of nanorod morphology at high Tb^{3+} levels, having already been discussed in XRD and SEM investigations in detail. Moreover, SEM analysis showed that TZ05 possesses a less dense nanorod network compared with EZ05, leading to a relatively smaller effective sensing surface area and consequently slightly lower sensitivity as compared to that of the Er-doped counterpart.

Table 3 CO_2 sensitivity of pure and doped ZnO nanorods at different gas concentrations under optimum temperatures

Sample	Sensitivity (%ΔR/R)					
	1 ppm	5 ppm	10 ppm	25 ppm	50 ppm	100 ppm
Z0	13	14	11	16	32	36
EZ01	20	26	29	32	40	54
EZ03	121	139	157	194	234	289
EZ05	277	320	377	433	543	733
EZ07	101	117	136	157	172	209
TZ01	43	54	61	87	113	153
TZ03	96	118	168	222	248	300
TZ05	278	317	356	380	403	475
TZ07	63	83	123	141	176	196

All in all, the temperature-dependent CO_2 sensitivity results clearly display that rare-earth doping significantly improves the CO_2 sensing performance of ZnO nanorods by enhancing surface reactivity and charge transport processes. On this basis, the existence of optimum dopant concentration (particularly 5% for both Er and Tb) in the ZnO semiconducting matrix maximizes sensitivity and defines a favorable operating temperature window around 500 K. On the other hand, excess doping leads to morphological deterioration and crystal degradation, which ultimately limit gas-surface interactions and significantly degrade sensor performance.

After determining the optimum operating temperatures, the dynamic CO_2 sensing performance of pure and rare-earth-doped ZnO semiconducting nanorod sensors was systematically evaluated under stepwise CO_2 concentrations ranging from 1 to 100 ppm. Figs. 11–15 summarize the concentration-dependent response behavior, resistance modulation, and sensing kinetics of the sensors under realistic operating conditions, while Table 3 provides a quantitative comparison of sensitivity values.

The undoped ZnO sensor, measured at 420 K (Fig. 11), exhibits stable and repeatable response-recovery cycles, confirming good baseline stability and reversibility. However, its sensitivity remains relatively low across the entire concentration range, increasing modestly from 13% at 1 ppm to 36% at 100 ppm (Table 3). At low CO_2 concentrations (1–25 ppm), the response varies only slightly, displaying the limited density of active adsorption sites and weak modulation of the surface depletion layer in pristine ZnO nanorods. A more serious increase in sensitivity at higher concentrations (50–100 ppm) is attributed to increased surface coverage by CO_2 molecules and stronger electron withdrawal from the conduction band. In contrast,

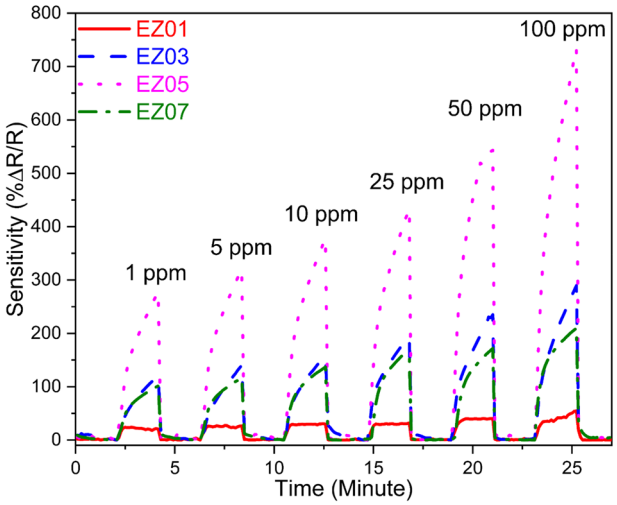

Fig. 12 Dynamic transient CO_2 gas-sensing response of the Er-doped ZnO nanorods (EZ series) under stepwise varying gas concentrations (1 to 100 ppm) measured at their respective optimal operating temperatures

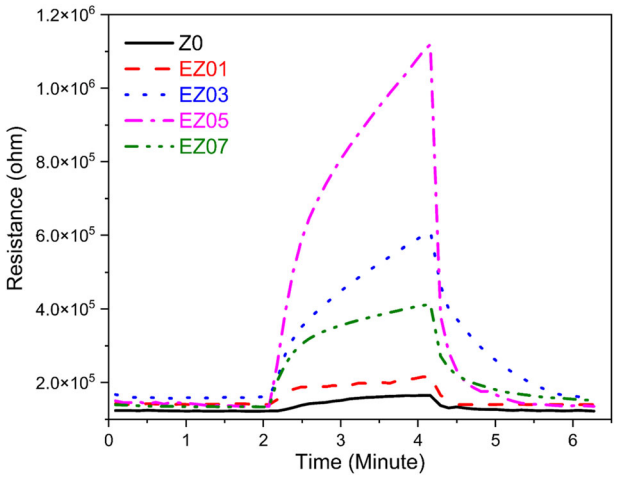

Fig. 13 Time-dependent electrical resistance modulation of the pure and Er-doped ZnO nanorods upon exposure to 100 ppm CO_2 gas, demonstrating the effect of Er incorporation on baseline resistance and charge transfer dynamics

Er^{3+}-doped ZnO nanorods exhibit a substantial and systematic increment in sensing performance (as provided in Fig. 12 and Fig. 13). For all Er-doped samples, sensitivity increases monotonically with CO_2 concentration, indicating effective concentration-dependent detection. Among the EZ series, the EZ05 sensor displays the best performance, achieving sensitivities of 277% at 1 ppm and 733% at 100 ppm. This exceptional response is associated with the synergistic effects of optimum Er incorporation, including increased oxygen vacancy concentration, a higher density of electron trapping sites, improved nanorod crystallinity, and enhanced grain-boundary potential barriers [108]. The features mentioned collectively intensify resistance modulation even at low gas concentrations, enabling superior trace-level

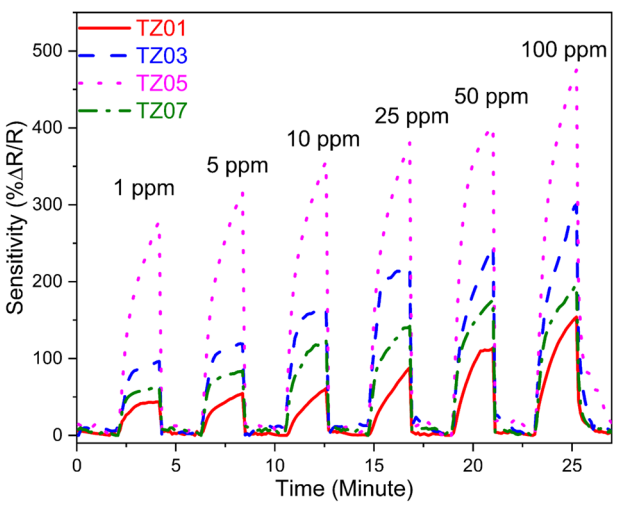

Fig. 14 Dynamic transient CO_2 gas-sensing response of the Tb-doped ZnO nanorods (TZ series) under stepwise varying gas concentrations (1 to 100 ppm) measured at their respective optimal operating temperatures

CO_2 detection. Resistance measurements under 100 ppm CO_2 exposure (see Fig. 13) further confirm that Er doping significantly amplifies resistance variation during gas adsorption, while the baseline resistance in an air environment (R_a) remains relatively unchanged. This is attributed to good electrical stability.

In the case of excess Er foreign content (EZ07) in the ZnO semiconducting structures, both sensitivity and resistance modulation decline, related to morphology degradation and defect clustering that limit effective gas-surface interactions. Moreover, the dynamic sensing characteristics of Tb-doped ZnO nanorods are presented in Figs. 14 and 15. Similar to the EZ series, the existence of Tb incorporation enhances CO_2 sensitivity as compared to that of pristine ZnO, and the response generally increases with gas concentration. Among the TZ series, the TZ05 sample exhibits the highest sensitivity of 278% at 1 ppm and 475% at 100 ppm. However, at similar concentrations, its performance remains lower than that of EZ05. The difference appeared in association with the lower nanorod density and reduced effective surface area observed in Tb-doped ZnO semiconducting compounds, which restricts gas adsorption and depletion-layer modulation. The TZ01 sample shows relatively weak sensitivity, indicating insufficient defect activation at low Tb incorporation levels, while the sensitivity of TZ07 decreases despite higher dopant content. This shows dopant-induced structural disorder and disrupted nanorod morphology. According to Fig. 15, the resistance variations under 100 ppm CO_2 exposure confirm that Tb doping modifies surface electronic states and enhances resistance modulation during gas exposure, although no strict linear dependence on dopant concentration is observed, in agreement with previous studies [42, 83, 84].

Compared with similar doping ratios reported in the literature, the relatively lower resistance values observed here [109] display improved charge transport pathways in the hydrothermally grown nanorod networks [42, 110].

To sum up, the combined dynamic response analysis and quantitative sensitivity data clearly indicate that doping with rare earth elements significantly improves the CO_2 sensing performance of ZnO semiconductor nanorods. In this context, the optimum dopant concentration for both Er and Tb foreign particles is approximately 5% by weight. Among all sensors investigated, Er-doped ZnO (especially the EZ05 semiconducting sample) exhibits the highest sensitivity, superior low-ppm detection capability, and strong scalability with gas concentration. These findings represent the critical role of controlled rare-earth incorporation in tailoring defect chemistry, morphology, and electronic structure to realize high-performance ZnO-based CO_2 sensors suitable for environmental monitoring and industrial sensing applications.

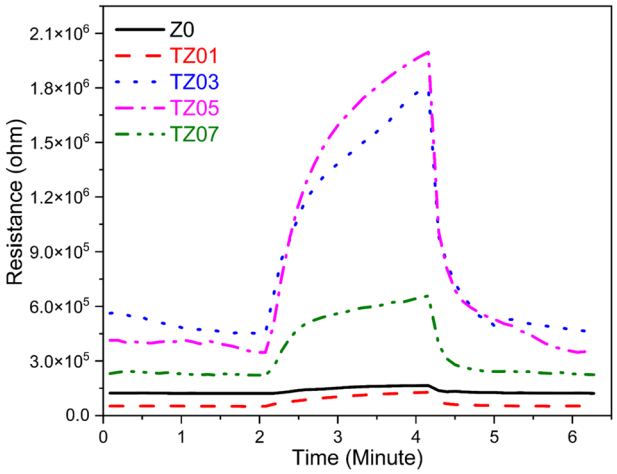

Fig. 15 Time-dependent electrical resistance modulation of the pure and Tb-doped ZnO nanorods upon exposure to 100 ppm CO_2 gas, illustrating the resistance variation during a complete adsorption-desorption cycle

The dynamic response curves were further analyzed to extract the key kinetic parameters of the sensors, namely the response and recovery times, which are critical for practical gas-sensing applications. The response time is defined as the duration required for the sensor to reach 90% of the total resistance change upon CO_2 exposure, whereas the recovery time corresponds to the period needed for the resistance to return to within 10% of its baseline value after removal of the target gas. The extracted values are summarized in Table 4.

Figure 16 compares the dynamic CO_2 sensitivity of pure ZnO with the optimally doped Er- (EZ05) and Tb-doped (TZ05) ZnO nanorod sensors under identical gas concentrations. Both EZ05 and TZ05 exhibit significantly enhanced sensitivity compared with the undoped sample, confirming the beneficial role of rare-earth incorporation in activating surface states and strengthening depletion-layer modulation. At low CO_2 concentrations (1–25 ppm), EZ05 and TZ05 show comparable sensitivity levels, showing that both dopants effectively promote gas adsorption and initial charge transfer. However, at higher concentrations (50–100 ppm), EZ05 clearly outperforms the TZ05 sample, displaying a steeper response increase. This behavior displays that Er doping produces a more stable and chemically active surface, enabling stronger interaction with CO_2 molecules and more efficient modulation of surface potential barriers. The reduced lattice distortion and improved crystallographic stability induced by Er^{3+} ions further contribute to this enhanced high-concentration response.

Figure 17 presents a direct comparison of sensitivity, response time, and recovery time for EZ05 and TZ05 at 100 ppm CO_2, where both sensors exhibit their strongest responses. The EZ05 sensor indicates not only higher sensitivity but also shorter response and recovery times compared with the TZ05 compound. This superior dynamic behavior indicates faster adsorption-desorption kinetics and more efficient charge transport pathways in the Er-doped nanorod network. Conversely, the inclusion of Tb^{3+} ions enhances sensitivity compared to pure ZnO semiconducting material but leads to relatively longer response times; this may be

Table 4 Response and recovery times of all ZnO nanorods at optimum operating conditions

Sample	1ppm		5ppm		10ppm		25ppm		50ppm		100ppm	
	Res.	Rec.	Res.	Rec.	Res.	Rec.	Res.	Rec.	Res.	Rec.	Res.	Rec.
EZ01	110	103	111	92	105	91	105	84	101	79	98	77
EZ03	108	58	107	55	102	46	97	40	97	21	91	21
EZ05	94	78	94	78	94	89	81	71	95	72	88	59
EZ07	100	60	100	60	100	61	100	61	105	54	104	35
TZ01	56	32	78	44	86	40	89	56	91	72	99	84
TZ03	61	34	54	32	57	34	64	39	87	58	96	73
TZ05	63	83	56	77	70	77	73	97	88	59	94	77
TZ07	100	79	94	78	94	77	94	86	75	81	93	87

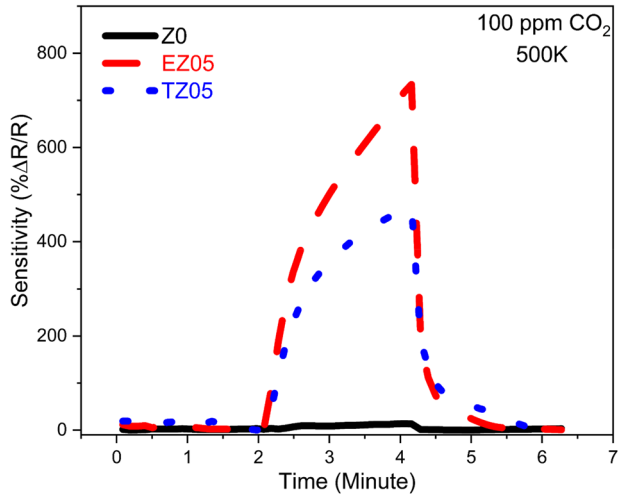

Fig. 16 Comparative dynamic CO_2 sensing response curves of the pure (Z0) and optimally doped samples (5 wt% Er: EZ05 and 5 wt% Tb: TZ05) at various gas concentrations evaluated at 500 K

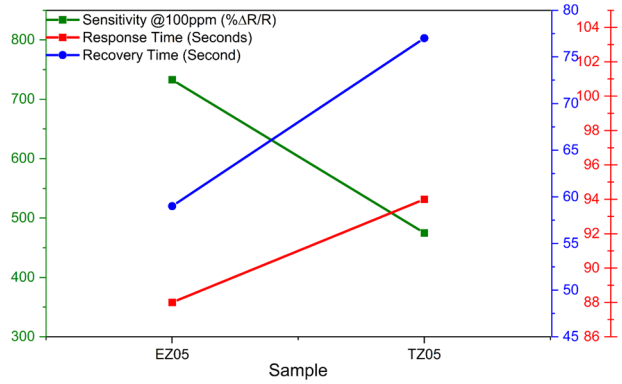

Fig. 17 Quantitative comparison of the maximum sensitivity, response time, and recovery time between the optimally doped EZ05 and TZ05 nanorods upon exposure to 100 ppm CO_2 gas

related to deeper trap states and slower surface reaction kinetics. The trends observed in Table 4 further support the observations. Increasing Er content generally leads to reduced response times, revealing accelerated electron exchange during gas adsorption, whereas Tb-doped ZnO semiconducting compounds tend to exhibit longer response times. Recovery times show an inverse trend, indicating that stronger gas-surface binding and deeper trap levels slow desorption processes. The balance between fast response and reasonable recovery is most favorably achieved in the EZ05 sample, emphasizing its superior kinetic performance.

With the aid of the combined evaluation of XRD and SEM results, we define critical information about the structural origin of the superior gas-sensing performance observed for the EZ05 semiconducting sample. As summarized in Table 1, EZ05 exhibits one of the largest nanorod apparent diameters measured by SEM (≈ 68.97 nm), while simultaneously possessing one of the smallest crystallite sizes determined from XRD analysis (D ≈ 37.61 nm). This apparent discrepancy indicates that the ZnO nanorods are not single crystalline but rather composed of multiple nanoscale crystallites, forming a polycrystalline nanorod architecture with a high density of internal grain boundaries.

In chemiresistive gas sensors, such grain boundaries are known to play a decisive role in sensing performance by acting as electron-trapping centers and forming potential energy barriers at intergranular junctions, having already been discussed in previous sections. Under ambient conditions, oxygen molecules adsorb preferentially at these grain boundaries and capture conduction-band electrons, forming ionized oxygen species (O_2^-/O^-) and increasing the height of the intergranular potential barriers, which leads to elevated sensor resistance. Upon exposure to CO_2, the interaction of gas molecules with the adsorbed oxygen species modulates the barrier height (discussed in the "Optical Analysis" section) and releases trapped electrons, leading to a significant change in resistance. Consequently, the high grain-boundary density in EZ05 provides a large number of active adsorption sites and enables stronger modulation of the depletion layer, directly contributing to its enhanced sensitivity and rapid response characteristics [108].

A comparison with previously reported ZnO-based CO_2 sensors further emphasizes the advantages of the present advanced system. As summarized in Table 5, many ZnO-based sensors reported in the literature operate effectively only at relatively high CO_2 concentrations or require additional activation mechanisms, such as UV illumination. For instance, Ca-doped ZnO sensors have been reported to exhibit a sensitivity of approximately 53% only at extremely high CO_2 concentrations (~ 50,000 ppm). Conversely, the EZ05 sensor developed in this study demonstrates an exceptionally high sensitivity of 733% at a low CO_2 concentration of 100 ppm, while operating at a moderate temperature of 500 K (227 °C). This substantial enhancement clearly displays that controlled Er incorporation not only optimizes the microstructural features of ZnO semiconducting nanorods but also significantly improves their low-concentration CO_2 detection capability, outperforming many previously reported ZnO-based sensing platforms. In conclusion, these results confirm that Er doping effectively tailors the structural and electronic properties of ZnO semiconducting nanorods, resulting in a highly efficient chemiresistive sensing mechanism suitable for sensitive and reliable CO_2 detection under relatively mild operating conditions.

4 Conclusion

In the current study, we examined the effects of rare-earth (Er and Tb) doping on the structural, morphological,

Table 5 Obtained results from studies in the literature on CO_2 gas detection

Material	Fabrication Method	Concentration of Applied Gas	Sensing Response	Temperature	Reference
3% Cd doped ZnO	chemical bath deposition	100 ppm	125 °C	88.24%	[107]
ZnO	chemical spray pyrolysis	400ppm	350 °C	65%	[111]
4.0% La doped ZnO	sol-gel spin coating	200 sccm	25 °C	122.71%	[112]
2.5% Na doped ZnO	sol-gel	50 sccm	25 °C	81.9%	[113]
5%In doped ZnO	sol-gel	100 ppm	200 °C	16%	[114]
ZnO	chemical bath deposition	2600 ppm	300 °C	17%	[115]
0.1% Mn doped ZnO	aerosol spray pyrolysis	100 ppm	25 °C (under UV)	66%	[116]
5% Ca doped ZnO	wet chemical synthesis	50000 ppm	350 °C	53%	[117]
5% Er doped ZnO	hydrothermal	100 ppm	227 °C	733%	In this work
5% Tb doped ZnO	hydrothermal	100 ppm	227 °CC	475%	In this work

optical, and CO_2 gas-sensing properties of hydrothermally synthesized ZnO nanorods with the aid of standard experimental measurements and theoretical approaches. XRD and SEM analyses confirmed that both Er^{3+} and Tb^{3+} ions were successfully incorporated into the hexagonal wurtzite ZnO lattice without disturbing the crystal structure up to an optimum doping level of 5 wt%, while higher dopant concentrations led to lattice distortion, secondary phase formation, and structural degradation. Growth in the *c*-direction was confirmed by the calculated diameter values, which were less than 100 nm. Besides, SEM images taken revealed that controlled rare-earth incorporation effectively modulated nanorod density, orientation, and diameter, with Er doping producing more uniform and densely packed nanorod arrays as compared to Tb doping. Additionally, optical measurements revealed a monotonic reduction in the band gap energy with increasing dopant concentration, which was attributed to band-gap shrinkage due to enhanced carrier concentration, defect-induced localized states, and dopant-host electronic interactions. The optical changes recorded further corroborated the successful incorporation of Er and Tb into the ZnO semiconducting lattice system and their influence on the electronic structure. At the same time, gas-sensing investigations revealed that rare-earth doping significantly enhances the CO_2 sensing performance of ZnO nanorods. Among all the doped series, the Er-doped ZnO nanorods with 5 wt% Er inclusions possessed the highest sensitivity (733% at 100 ppm CO_2), excellent response-recovery characteristics, and stable operation at a relatively low working temperature of 500 K. The superior sensing performance of EZ05 semiconductor was associated with its polycrystalline nanorod architecture with a high density of grain boundaries, optimized defect chemistry, increased oxygen vacancy concentration, and efficient modulation of intergranular potential barriers during gas exposure. Although Tb-doped ZnO nanorods also presented enhanced sensing performance compared to that of pure direct-transition-type ZnO semiconducting material, their sensitivity and dynamic response were comparatively lower, primarily due to less favorable morphology and dopant-induced structural disorder at higher concentrations.

To sum up, the theoretical results and experimental findings indicate that controlled Er doping is a highly effective strategy for shaping the microstructural and electronic properties of ZnO semiconducting nanorods to achieve high-performance, low-concentration CO_2 detection. The outstanding sensitivity, fast response, and moderate operating temperature of the EZ05 sensor emphasize its strong potential for practical environmental monitoring and industrial gas-sensing applications.

Data availability

All data generated or analysed during this study are included in this article.

Author contributions FB: Writing original draft, visualization, resources, preparing figures and investigation. ÖÖ: Formal analysis, conceptualization, and supervision. ŞÇ: Resources, Formal analysis and reviewed. GY: Review, editing, resources, and investigation. SA: Review, editing, validation, and investigation. All authors reviewed the manuscript.

Funding The authors received no financial support for the research or authorship of this article. The Open Access publication fee for this article was covered under the Read and Publish transformative agreement between TÜBİTAK ULAKBİM and Springer Nature, through the participation of the Sinop University Library. Open access funding provided by the Scientific and Technological Research Council of Türkiye (TÜBİTAK).

Compliance with ethical standards

Conflict of interest The authors declare no competing interests.

Publisher's note Springer Nature remains neutral with regard to jurisdictional claims in published maps and institutional affiliations.

References

1. Lüthi D, Le Floch M, Bereiter B et al. (2008) High-resolution carbon dioxide concentration record 650,000–800,000 years before present. Nature 453:379–382. https://doi.org/10.1038/nature06949
2. Sakurai G, Yonemura S, Kishimoto-Mo AW et al. (2015) Inversely estimating the vertical profile of the soil CO_2 production rate in a deciduous broadleaf forest using a particle filtering method. PLoS ONE 10:e0119001. https://doi.org/10.1371/journal.pone.0119001
3. Humlum O, Stordahl K, Solheim J-E (2013) The phase relation between atmospheric carbon dioxide and global temperature. Glob Planet Change 100:51–69. https://doi.org/10.1016/j.gloplacha.2012.08.008
4. Lin Y, Zeng Z, Chen L, Deng Z (2023) The relation between the CO_2 concentration levels and the temperature. E3S Web Conf 375:03014. https://doi.org/10.1051/e3sconf/202337503014
5. Sitch S, Brovkin V, von Bloh W, et al (2005) Impacts of future land cover changes on atmospheric CO $_2$ and climate. Global Biogeochem Cycles 19 https://doi.org/10.1029/2004GB002311
6. Molina A, Escobar-Barrios V, Oliva J (2020) A review on hybrid and flexible CO_2 gas sensors. Synth Met 270:116602. https://doi.org/10.1016/j.synthmet.2020.116602
7. Chao HJ, Schwartz J, Milton DK, Burge HA (2003) The work environment and workers' health in four large office buildings. Environ Health Perspect 111:1242–1248. https://doi.org/10.1289/ehp.5697
8. Erdmann CA, Apte MG (2004) Mucous membrane and lower respiratory building-related symptoms in relation to indoor carbon dioxide concentrations in the 100-building BASE dataset. Indoor Air 14:127–134. https://doi.org/10.1111/j.1600-0668.2004.00298.x
9. Peng Z, Jimenez JL (2021) Exhaled CO_2 as a COVID-19 infection risk proxy for different indoor environments and activities. Environ Sci Technol Lett 8:392–397. https://doi.org/10.1021/acs.estlett.1c00183
10. Rudnick SN, Milton DK (2003) Risk of indoor airborne infection transmission estimated from carbon dioxide concentration. Indoor Air 13:237–245. https://doi.org/10.1034/j.1600-0668.2003.00189.x
11. Mendell MJ, Eliseeva EA, Davies MM et al. (2013) Association of classroom ventilation with reduced illness absence: a prospective study in California elementary schools. Indoor Air 23:515–528. https://doi.org/10.1111/ina.12042
12. Seiyama T (1988) Chemical Sensors —Current State and Future Outlook. In: SEIYAMA T (ed) Chemical Sensor Technology. Elsevier, Amsterdam, pp 1–13 https://doi.org/10.1016/B978-0-444-98901-7.50006-3
13. Karthik TVK, Martínez-García H, Ortiz-Chi F et al. (2023) CO_2 gas sensing properties of graphitic carbon nitride (g-C3N4) thin films. Diam Relat Mater 133:109736. https://doi.org/10.1016/j.diamond.2023.109736
14. Skouloudis AN, Kassomenos P (2014) Combining environment and health information systems for the assessment of atmospheric pollution on human health. Sci Total Environ 488–489:362–368. https://doi.org/10.1016/j.scitotenv.2014.02.116
15. Penza M, Suriano D, Cassano G et al. (2015) A case-study of microsensors for landfill air-pollution monitoring applications. Urban Clim 14:351–369. https://doi.org/10.1016/j.uclim.2014.09.002
16. Andò B, Baglio S, Di Pasquale G et al. (2015) An inkjet printed CO_2 gas sensor. Procedia Eng 120:628–631. https://doi.org/10.1016/j.proeng.2015.08.755
17. Baranov A, Spirjakin D, Akbari S, Somov A (2015) Optimization of power consumption for gas sensor nodes: a survey. Sens Actuators A Phys 233:279–289. https://doi.org/10.1016/j.sna.2015.07.016
18. Sheng-Joue Y (2014) Photoconductive gain and noise properties of ZnO nanorods schottky barrier photodiodes. IEEE J Sel Top Quantum Electron 20:96–99. https://doi.org/10.1109/JSTQE.2014.2316599
19. Shih WS, Young SJ, Ji LW et al (2011) Effect of oxygen plasma treatment on characteristics ofTiO$_{2}$photodetectors. IEEE Sens J 11:3031–3035. https://doi.org/10.1109/JSEN.2011.2150212
20. Wang C, Yin L, Zhang L et al. (2010) Metal oxide gas sensors: sensitivity and influencing factors. Sensors 10:2088–2106. https://doi.org/10.3390/s100302088
21. Zhou L, Bai J, Liu Y et al. (2020) Highly sensitive C2H2 gas sensor based on Ag modified ZnO nanorods. Ceram Int 46:15764–15771. https://doi.org/10.1016/j.ceramint.2020.03.120
22. Lu G, Xu J, Sun J et al. (2012) UV-enhanced room temperature NO2 sensor using ZnO nanorods modified with SnO2 nanoparticles. Sens Actuators B Chem 162:82–88. https://doi.org/10.1016/j.snb.2011.12.039
23. Bagheri M, Hamedani NF, Mahjoub AR et al. (2014) Highly sensitive and selective ethanol sensor based on Sm2O3-loaded flower-like ZnO nanostructure. Sens Actuators B Chem 191:283–290. https://doi.org/10.1016/j.snb.2013.10.001
24. Kamble VS, Navale YH, Patil VB et al. (2021) Enhanced NO2 gas sensing performance of Ni-doped ZnO nanostructures. J Mater Sci Mater Electron 32:2219–2233. https://doi.org/10.1007/s10854-020-04987-z
25. Arun Kumar KD, Valanarasu S, Ponraj JS et al. (2020) Effect of Er doping on the ammonia sensing properties of ZnO thin films prepared by a nebulizer spray technique. J Phys Chem Solids 144:109513. https://doi.org/10.1016/j.jpcs.2020.109513
26. Gómez-Pozos H, Arredondo E, Maldonado Álvarez A et al. (2016) Cu-doped ZnO thin films deposited by a sol-gel process using two copper precursors: gas-sensing performance in a propane atmosphere. Materials 9:87. https://doi.org/10.3390/ma9020087
27. Kumar RD, Nagarani S, Balachandran S et al. (2022) High-performing hexagonal-shaped ZnO nanopowder for Pseudo-supercapacitors applications. Surf Interfaces 33:102203. https://doi.org/10.1016/j.surfin.2022.102203
28. Hu Y, Zhou X, Han Q et al. (2003) Sensing properties of CuO–ZnO heterojunction gas sensors. Mater Sci Eng B 99:41–43. https://doi.org/10.1016/S0921-5107(02)00446-4
29. Nagarani S, Sasikala G, Yuvaraj M et al. (2022) ZnO-CuO nanoparticles enameled on reduced graphene nanosheets as electrode materials for supercapacitor applications. J Energy Storage 52:104969. https://doi.org/10.1016/j.est.2022.104969
30. Sandhiran N, Ganapathy S, Manoharan Y et al. (2022) CuO–NiO binary transition metal oxide nanoparticle anchored on rGO

nanosheets as a high-performance electrocatalyst for the oxygen reduction reaction. Environ Res 211:112992. https://doi.org/10.1016/j.envres.2022.112992
31. Shin J, Choi S-W, Kim C et al. (2025) Characterization and H2S gas sensing characteristics of Au-decorated ZnO nanorods prepared by a two-step wet method. J Alloy Compd 1021:179655. https://doi.org/10.1016/j.jallcom.2025.179655
32. Patil VL, Bhosale SR, Bhosale RR et al. (2023) Low temperature chemiresistive gas sensing performance towards oxidizing gas based on chemically prepared Ga doped ZnO nanorods. Inorg Chem Commun 152:110691. https://doi.org/10.1016/j.inoche.2023.110691
33. Patil VL, Dalavi DS, Dhavale SB et al. (2022) NO2 gas sensing properties of chemically grown Al-doped ZnO nanorods. Sens Actuators A Phys 340:113546. https://doi.org/10.1016/j.sna.2022.113546
34. Tepliakova I, Abid M, Viter R et al. (2026) 1D ZnO Nanostructures in analytical systems for Cu(II) and Fe(III) ion sensing. ACS Appl Nano Mater 9:3664–3678. https://doi.org/10.1021/acsanm.5c05081
35. Choi KJ, Jang HW (2010) One-dimensional oxide nanostructures as gas-sensing materials: review and issues. Sensors 10:4083–4099. https://doi.org/10.3390/s100404083
36. Godse PR, Kadam SA, Nimbalkar TM et al. (2024) Ultra-responsive and highly sensitive 1D ZnO nanotubes for detecting perilous low levels of NO_2 gas. Mater Adv 5:2826–2840. https://doi.org/10.1039/D3MA00962A
37. Panda SA, Barala S, Hazra A, Gangopadhyay S (2025) Modulation of 1D ZnO nanostructures for selective formaldehyde sensing: The role of surface energy, polarization, and adatom kinetics toward asymmetric growth. Ceram Int 51:45678–45690. https://doi.org/10.1016/j.ceramint.2025.07.283
38. Zayas-Bazán PG, Galdámez-Martínez A, Lugo-Ruiz D et al. (2025) High-performance acetone detection via one-dimensional sulfur-doped ZnO nanostructures. Sens Actuators A Phys 387:116365. https://doi.org/10.1016/j.sna.2025.116365
39. González-Garnica M, Galdámez-Martínez A, Malagón F et al. (2021) One-dimensional Au-ZnO hybrid nanostructures based CO_2 detection: growth mechanism and role of the seed layer on sensing performance. Sens Actuators B Chem 337:129765. https://doi.org/10.1016/j.snb.2021.129765
40. Hastir A, Kohli N, Singh RC (2017) Comparative study on gas sensing properties of rare earth (Tb, Dy and Er) doped ZnO sensor. J Phys Chem Solids 105:23–34. https://doi.org/10.1016/j.jpcs.2017.02.004
41. Chen T-P, Chang S-P, Hung F-Y et al. (2013) Simple fabrication process for 2D ZnO nanowalls and their potential application as a methane sensor. Sensors 13:3941–3950. https://doi.org/10.3390/s130303941
42. Sebastian S, Raj CSA, Diana P et al. (2024) Rare earth elements terbium (Tb), erbium (Er), ytterbium (Yb) doped zinc oxide nanoparticles: synthesis structural optical and gas sensing studies. Phys B Condens Matter 694:416384. https://doi.org/10.1016/j.physb.2024.416384
43. Shkir M, Ben Gouider Trabelsi A, Alkallas FH, AlFaify S (2022) High performance of the rare earth (Er, Gd & Pr) doped MoO3 thin films for advanced applications towards ammonia gas sensing. J Mater Res Technol 20:4556–4565. https://doi.org/10.1016/j.jmrt.2022.08.144
44. Flor J, deLima SAM, Davolos MR (2004) Effect of reaction time on the particle size of ZnO and ZnO: Ce obtained by a sol–gel method. In: Surface and Colloid Science. Springer Berlin Heidelberg, Berlin
45. Shukla S, Sharma DK (2021) A review on rare earth (Ce and Er)-doped zinc oxide nanostructures. Mater Today Proc 34:793–801. https://doi.org/10.1016/j.matpr.2020.05.264
46. Meng JX, Cheah KW, Shi ZP, Li JQ (2007) Intense 1540nm emission from Er-doped Ce: YAG phosphor. Appl Phys Lett 91 https://doi.org/10.1063/1.2785136
47. Lakshminarayana G, Vidya Sagar R, Buddhudu S (2008) NIR luminescence from Er3+/Yb3+, Tm3+/Yb3+, Er3+/Tm3+ and Nd3+ ions-doped zincborotellurite glasses for optical amplification. J Lumin 128:690–695. https://doi.org/10.1016/j.jlumin.2007.11.081
48. Pérez-Casero R, Gutiérrez-Llorente A, Pons-Y-Moll O, et al (2005) Er-doped ZnO thin films grown by pulsed-laser deposition. J Appl Phys 97 https://doi.org/10.1063/1.1858058
49. Takahei K, Taguchi A (1993) Selective formation of an efficient Er-O luminescence center in GaAs by metalorganic chemical vapor deposition under an atmosphere containing oxygen. J Appl Phys 74:1979–1982. https://doi.org/10.1063/1.354757
50. Polman A (1997) Erbium-implanted thin film photonic materials. J Appl Phys 82:1–39. https://doi.org/10.1063/1.366265
51. Galdámez-Martinez A, Santana G, Güell F et al. (2020) Photoluminescence of ZnO nanowires: a review. Nanomaterials 10:857. https://doi.org/10.3390/nano10050857
52. Shivaraj B, Prabhakara MC, Bhojya Naik HS et al. (2023) Fabrication of Tb-doped ZnO nanoparticle via co-precipitation technique for multifunctional applications. Chem Phys Lett 818:140421. https://doi.org/10.1016/j.cplett.2023.140421
53. Naik EI, Naik HSB, Viswanath R et al. (2020) Bright red luminescence emission of macroporous honeycomb-like Eu3+ ion-doped ZnO nanoparticles developed by gel-combustion technique. SN Appl Sci 2:863. https://doi.org/10.1007/s42452-020-2639-x
54. Hastir A, Opila RL, Kohli N et al. (2017) Deposition, characterization and gas sensor application of RF magnetron-sputtered terbium-doped ZnO films. J Mater Sci 52:8502–8517. https://doi.org/10.1007/s10853-017-1059-9
55. Singh P, Kumar R, Singh RK (2020) Fabrication of Co- and Ce-doped ZnO nanoparticles: a structural, morphological and optical properties investigation. Appl Nanosci 10:1231–1241. https://doi.org/10.1007/s13204-019-01217-9
56. Yang YH, Zhu HG, Dong HM, Yang GW (2014) Growth and luminescence of Tb-doped ZnO nanocones. Mater Lett 124:32–35. https://doi.org/10.1016/j.matlet.2014.03.031
57. Pathak TK, Coetsee-Hugo E, Swart HC et al. (2020) Preparation and characterization of Ce-doped ZnO nanomaterial for photocatalytic and biological applications. Mater Sci Eng: B 261:114780. https://doi.org/10.1016/j.mseb.2020.114780
58. Chelouche A, Touam T, Djouadi D, Aksas A (2014) Synthesis and characterizations of new morphological ZnO and Ce-doped ZnO powders by sol–gel process. Optik 125:5626–5629. https://doi.org/10.1016/j.ijleo.2014.06.072
59. Juang F-R, Chen B-Y (2020) Effect of adding ZHS microcubes on ZnO nanorods for CO_2 gas sensing applications. Solid State Electron 164:107711. https://doi.org/10.1016/j.sse.2019.107711
60. Radhakrishnan JK, Kumara M, Geetika (2021) Effect of temperature modulation, on the gas sensing characteristics of ZnO nanostructures, for gases O_2, CO and CO_2. Sens Int 2:100059. https://doi.org/10.1016/j.sintl.2020.100059
61. Kaya S, Ozturk O, Arda L (2022) Correlation between crystal defects and room temperature ferromagnetism of hydrothermally grown Eu-substituted ZnO nanorods. Phys B Condens Matter 645:414281. https://doi.org/10.1016/j.physb.2022.414281
62. Ajjaq A, Bulut F, Ozturk O, Acar S (2024) Advanced NH3 detection by 1D nanostructured La:ZnO sensors with novel intrinsic p–n shifting and ultrahigh baseline stability. ACS Sens 9:895–911. https://doi.org/10.1021/acssensors.3c02256
63. Bulut F, Ozturk Ö, Acar S, Yildirim G (2022) Effect of Ni and Al doping on structural, optical, and CO gas sensing properties of 1D ZnO nanorods produced by hydrothermal method.

Microsc Res Tech 85:1502–1517. https://doi.org/10.1002/jemt.24013
64. Çağırtekin AO, Acar S (2025) NH3 gas sensing with pure and Y-doped ZnO nanoflowers synthesized by the hydrothermal method. Ceram Int 51:18305–18314. https://doi.org/10.1016/j.ceramint.2025.02.011
65. Ghanem MG, Badr Y, Hameed TA, et al (2019) Synthesis and characterization of undoped and Er-doped ZnO nano-structure thin films deposited by sol-gel spin coating technique. Mater Res Express 6 https://doi.org/10.1088/2053-1591/ab2750
66. Çağırtekin AO, Ajjaq A, Barin Ö, Acar S (2023) Temperature-dependent dielectric properties of p-n heterojunction diodes based on hydrothermally synthesized ZnO nanostructures. Phys Scr 98:105949. https://doi.org/10.1088/1402-4896/acf80e
67. Chen J, Zhu W, Gao Y et al. (2019) Electroluminescence from light-emitting devices based on erbium-doped ZnO/n-Si heterostructures: enhancement effect of fluorine co-doping. Opt Express 27:30919. https://doi.org/10.1364/OE.27.030919
68. Portillo-Cortez K, Islas SR, Serrano-Lázaro A et al. (2022) A novel soft deposition methodology for textured ZnO: Al thin films as efficient transparent conductive oxide layers. Appl Surf. Sci Adv 9:100255. https://doi.org/10.1016/j.apsadv.2022.100255
69. Portillo-Cortez K, Martínez A, Bizarro M, et al (2021) ZnO nanowires/N719 dye with different aspect ratios as a possible photoelectrode for dye-sensitized solar cells. Front Chem 8 https://doi.org/10.3389/fchem.2020.604092
70. Molefe FV, Mofokeng SJ, Khenfouch M et al. (2019) The effect of Zn $^{2+}$ on the anion vacancies in ZnO thin-films grown using chemical bath deposition. J Phys Conf Ser 1292:012016. https://doi.org/10.1088/1742-6596/1292/1/012016
71. Luo L, Gong L, Liu YF et al. (2010) Enhanced ultraviolet lasing from europium-doped zinc oxide nanocrystals. Opt Mater 32:1066–1070. https://doi.org/10.1016/j.optmat.2010.02.032
72. Ahammed N, Hassan MS, Hassan M (2018) Effects of aluminum (Al) incorporation on structural, optical and thermal properties of ZnO nanoparticles. Mater Sci-Pol 36:419–426. https://doi.org/10.1515/msp-2018-0018
73. Guang-Lei T, Hong-Bo HE, Jian-Da S (2005) Effect of microstructure of TiO₂ thin films on optical band gap energy. Chin Phys Lett 22:1787–1789
74. Yildirim G, Bal S, Gulen M et al. (2012) Substrate effect on microstructure and optical performance of sputter-deposited TiO $_2$ thin films. Cryst Res Technol 47:195–201. https://doi.org/10.1002/crat.201100614
75. Jiu J, Wang F, Adachi M (2004) Preparation of highly photocatalytic active nano-scale TiO2 by mixed template method. Mater Lett 58:3915–3919. https://doi.org/10.1016/j.matlet.2004.08.017
76. Buryi M, Remeš Z, Hájek F et al. (2023) Peculiarities related to Er doping of ZnO nanorods simultaneously grown as particles and vertically arranged arrays. J Phys Chem C 127:22177–22189. https://doi.org/10.1021/acs.jpcc.3c05471
77. Buryi M, Remeš Z, Babin V et al. (2021) Transformation of free-standing ZnO nanorods upon Er doping. Appl Surf Sci 562:150217. https://doi.org/10.1016/j.apsusc.2021.150217
78. Arda L (2019) The effects of Tb-doped ZnO nanorod: an EPR study. J Magn Magn Mater 475:493–501. https://doi.org/10.1016/j.jmmm.2018.11.121
79. Otal EH, Yoon S, Aguirre M, Weidenkaff A (2011) Metastability of heavy lanthanides in the ZnO wurtzite structure. J Alloy Compd 509:S364–S366. https://doi.org/10.1016/j.jallcom.2011.02.076
80. Liu S-M, Liu F-Q, Wang Z-G (2001) Relaxation of carriers in terbium-doped ZnO nanoparticles. Chem Phys Lett 343:489–492. https://doi.org/10.1016/S0009-2614(01)00740-0
81. Korsunska N, Borkovska L, Khomenkova L et al. (2020) Redistribution of Tb and Eu ions in ZnO films grown on different substrates under thermal annealing and its impact on Tb-Eu energy transfer. Appl Surf Sci 528:146913. https://doi.org/10.1016/j.apsusc.2020.146913
82. Ghomri R, Shaikh MN, Ahmed MI, et al (2016) (Al, Er) co-doped ZnO nanoparticles for photodegradation of rhodamine blue. Appl Phys A Mater Sci Process 122 https://doi.org/10.1007/s00339-016-0417-9
83. Sharma DK, Sharma KK, Kumar V, Sharma A (2018) Synthesis of Er-doped ZnO cone-like nanostructures with enhanced structural, optical and magnetic properties. J Mater Sci: Mater Electron 29:3840–3849. https://doi.org/10.1007/s10854-017-8320-5
84. Zamiri R, Lemos AF, Reblo A et al. (2014) Effects of rare-earth (Er, La and Yb) doping on morphology and structural properties of ZnO nanostructures prepared by wet chemical method. Ceram Int 40:523–529. https://doi.org/10.1016/j.ceramint.2013.06.034
85. Panwar V, Sharma KK, Tewari A (2026) Sintering behavior and thermoelectric properties of Al- and Mg-doped ZnO: effect of grain boundary segregation. Int J Appl Ceram Technol 23 https://doi.org/10.1111/ijac.70168
86. Yadav N, Parker SC, Tewari A (2024) Genetic algorithm-assisted multiscale modeling of grain boundary segregation of Al in ZnO and its correlation with nominal dopant concentration. J Eur Ceram Soc 44:944–953. https://doi.org/10.1016/j.jeurceramsoc.2023.09.050
87. Panwar V, Yadav N, Rowthu S, Tewari A (2025) Atomistic modeling and experimental study of dopant segregation-induced morphology transition in ZnO nanoparticles. J Am Ceramic Soc 108 https://doi.org/10.1111/jace.20636
88. Sulaiman S, Sudin I, Al-Naib UMB, Omar MF (2022) Review of the nanostructuring and doping strategies for high-performance zno thermoelectric materials. Crystals 12:1076. https://doi.org/10.3390/cryst12081076
89. Nasr B, Dasgupta S, Wang D, et al (2010) Electrical resistivity of nanocrystalline Al-doped zinc oxide films as a function of Al content and the degree of its segregation at the grain boundaries. J Appl Phys 108 https://doi.org/10.1063/1.3511346
90. Yang L-C, Jung D-R, Po F-R et al. (2020) Tailoring bandgap and electrical properties of magnesium-doped aluminum zinc oxide films deposited by reactive sputtering using metallic Mg and Al–Zn targets. Coatings 10:708. https://doi.org/10.3390/coatings10080708
91. Yamada T, Makino H, Yamamoto N, Yamamoto T (2010) Ingrain and grain boundary scattering effects on electron mobility of transparent conducting polycrystalline Ga-doped ZnO films. J Appl Phys 107 https://doi.org/10.1063/1.3447981
92. Ghrib T, Massoudi I, Al-Otaibi AL et al. (2021) Effects of terbium doping on structural, optical and photocatalytic properties of ZnO nanopowder prepared by solid-state reaction. J Inorg Organomet Polym Mater 31:239–250. https://doi.org/10.1007/s10904-020-01761-w
93. Adhyapak PV, Bharatula LD, Rathi A, et al (2017) Influence of erbium doping on hydrothermally synthesized ZnO nanostructures and their enhanced gas sensing properties. Current Smart Materials 2 https://doi.org/10.2174/2405465802666170517150820
94. Bura M, Singh G, Gupta D et al. (2022) Transition in the preferred orientation of RF sputtered ZnO/Si thin films by thermal annealing: Structural, morphological, and optical characteristics. Opt Mater (Amst) 133:113024. https://doi.org/10.1016/j.optmat.2022.113024
95. Honglin L, Yingbo L, Jinzhu L, Ke Y (2014) Experimental and first-principles studies of structural and optical properties of rare earth (RE = La, Er, Nd) doped ZnO. J Alloy Compd 617:102–107

96. Achehboune M, Khenfouch M, Boukhoubza I, et al (2022) A DFT study on the electronic structure, magnetic and optical properties of Er-doped ZnO: effect of Er concentration and native defects. Comput Condens Matter 31 https://doi.org/10.1016/j.cocom.2021.e00627
97. Zamiri R, Kaushal A, Rebelo A, Ferreira JMF (2014) Er-doped ZnO nanoplates: synthesis, optical and dielectric properties. Ceram Int 40:1635–1639. https://doi.org/10.1016/j.ceramint.2013.07.054
98. Yergaliuly G, Tangirbergen A, Mentbayeva A, et al (2025) Advanced surface engineering of TZO nanostructures via irradiation technique for enhanced nitric oxide (NO) gas sensitivity. Appl Surface Sci Adv 27 https://doi.org/10.1016/j.apsadv.2025.100736
99. Aggarwal N, Vasishth A, Kaur K, Verma NK (2019) Investigation of optical, electrical and magnetic properties of Tb-doped ZnO nanorods. J Mater Sci Mater Electron 30:4807–4812. https://doi.org/10.1007/s10854-019-00774-7
100. Asikuzun Tokeser E, Ozturk O, Kurnaz S et al. (2023) A detailed research for determination of Er/Gd co-doping effect in ZnO-NPs thin films on optical, electrical and crystallographic properties. J Mater Sci Mater Electron 34:135. https://doi.org/10.1007/s10854-022-09585-9
101. Bayan S, Das U, Mohanta D (2010) Development of Tb-doped ZnO nanorods: effect of nitrogen ion irradiation on luminescence and structural evolution. Phys Status Solidi (A) Appl Mater Sci 207:1859–1863. https://doi.org/10.1002/pssa.200925525
102. Iordanova R, Gegova R, Bachvarova-Nedelcheva A, Dimitriev Y (2015) Sol-gel synthesis of composites in the ternary TiO2–TeO2–B2O3 system. Phys Chem Glasses Eur J Glass Sci Technol Part B 56:128–138. https://doi.org/10.13036/17533562.56.4.128
103. Farhat S, Rekaby M, Awad R (2018) Synthesis and characterization of Er-doped nano ZnO samples. J Supercond Nov Magn 31:3051–3061. https://doi.org/10.1007/s10948-017-4548-9
104. Rakhmanova A, Soltabayev B, Ajjaq A et al. (2025) Nanofibrous ZnO-loaded PVA/PEDOT: PSS for selective and enhanced ammonia detection. Sens Actuators B Chem 426:137022. https://doi.org/10.1016/j.snb.2024.137022
105. Ahlers S, Müller G, Doll T (2005) A rate equation approach to the gas sensitivity of thin film metal oxide materials. Sens Actuators B Chem 107:587–599. https://doi.org/10.1016/j.snb.2004.11.020
106. Barin Ö, Ajjaq A, Çağırtekin AO et al. (2022) Pivotal role of nucleation layers in the hydrothermally-assisted growth of ZnO and its H2 gas sensing performance. Sens Actuators B Chem 371:132499. https://doi.org/10.1016/j.snb.2022.132499
107. Altun B, Karaduman Er I, Çağırtekin AO et al. (2021) Effect of Cd dopant on structural, optical and CO_2 gas sensing properties of ZnO thin film sensors fabricated by chemical bath deposition method. Appl Phys A 127:687. https://doi.org/10.1007/s00339-021-04843-9
108. Al-Hashem M, Akbar S, Morris P (2019) Role of oxygen vacancies in nanostructured metal-oxide gas sensors: a review. Sens Actuators B Chem 301:126845. https://doi.org/10.1016/j.snb.2019.126845
109. Wei T, Li W, Zhang J, Xie X (2023) Synthesis of Tb2O3/ZnO composite nanofibers via electrospinning as chemiresistive gas sensor for detecting NO gas. J Alloy Compd 947:169651. https://doi.org/10.1016/j.jallcom.2023.169651
110. Sharma A, Rai VN (2019) A study of surface defects in TB doped zno nanoparticles for gas sensing applications. AIP Conference Proceedings: 2100 https://doi.org/10.1063/1.5098595
111. Hunge YM, Yadav AA, Kulkarni SB, Mathe VL (2018) A multifunctional ZnO thin film based devices for photoelectrocatalytic degradation of terephthalic acid and CO2 gas sensing applications. Sens Actuators B Chem 274:1–9. https://doi.org/10.1016/j.snb.2018.07.117
112. Abdelkarem K, Saad R, El Sayed AM et al. (2023) Design of high-sensitivity La-doped ZnO sensors for CO2 gas detection at room temperature. Sci Rep 13:18398. https://doi.org/10.1038/s41598-023-45196-y
113. Basyooni MA, Shaban M, El Sayed AM (2017) Enhanced gas sensing properties of spin-coated Na-doped ZnO nanostructured films. Sci Rep 7:41716. https://doi.org/10.1038/srep41716
114. Shokry Hassan H, Kashyout AB, Morsi I et al. (2014) Synthesis, characterization and fabrication of gas sensor devices using ZnO and ZnO: In nanomaterials. Beni Suef Univ J Basic Appl Sci 3:216–221. https://doi.org/10.1016/j.bjbas.2014.10.007
115. Dhawale DS, Lokhande CD (2011) Chemical route to synthesis of mesoporous ZnO thin films and their liquefied petroleum gas sensor performance. J Alloy Compd 509:10092–10097. https://doi.org/10.1016/j.jallcom.2011.08.046
116. Motaung DE, Kortidis I, Mhlongo GH et al. (2016) Correlating the magnetism and gas sensing properties of Mn-doped ZnO films enhanced by UV irradiation. RSC Adv 6:26227–26238. https://doi.org/10.1039/C5RA27154A
117. Ghosh A, Zhang C, Shi S, Zhang H (2019) High temperature CO_2 sensing and its cross-sensitivity towards H_2 and CO gas using calcium-doped ZnO thin film coated langasite SAW sensor. Sens Actuators B Chem 301 https://doi.org/10.1016/j.snb.2019.126958